remote sensing

MDPI

Article

Analysis of High-Frequency Sea-State Variability Using SWOT Nadir Measurements and Application to Altimeter Sea State Bias Modelling

Estelle Mazaleyrat [1,*], Ngan Tran [1], Laïba Amarouche [1], Douglas Vandemark [2,3], Hui Feng [2,3], Gérald Dibarboure [4] and François Bignalet-Cazalet [4]

[1] Collecte Localisation Satellites, 11 Rue Hermès, 31520 Ramonville Saint-Agne, France
[2] Ocean Process Analysis Laboratory, Institute for the Study of Earth, Oceans, and Space, University of New Hampshire, Durham, NH 03824, USA
[3] Global Science & Technology, Inc., Greenbelt, MD 20770, USA
[4] Centre National d'Etudes Spatiales, 31400 Toulouse, France
* Correspondence: emazaleyrat@groupcls.com

Abstract: The 1-day fast-sampling orbit phase of the Surface Water Ocean Topography (SWOT) satellite mission provides a unique opportunity to analyze high-frequency sea-state variability and its implications for altimeter sea state bias (SSB) model development. Time series with 1-day repeat sampling of sea-level anomaly (SLA) and SSB input parameters—comprising the significant wave height (SWH), wind speed (WS), and mean wave period (MWP)—are constructed using SWOT's nadir altimeter data. The analyses corroborate the following key SSB modelling assumption central to empirical developments: the SLA noise due to all factors, aside from sea state change, is zero-mean. Global variance reduction tests on the SSB model's performance using corrected SLA differences show that correction skill estimation using a specific (1D, 2D, or 3D) SSB model is unstable when using short time difference intervals ranging from 1 to 5 days, reaching a stable asymptotic limit after 5 days. It is proposed that this result is related to the temporal auto- and cross-correlations associated with the SSB model's input parameters; the present study shows that SSB wind-wave input measurements take time (typically 1–4 days) to decorrelate in any given region. The latter finding, obtained using unprecedented high-frequency satellite data from multiple ocean basins, is shown to be consistent with estimates from an ocean wave model. The results also imply that optimal time-differencing (i.e., >4 days) should be considered when building SSB model data training sets. The SWOT altimeter data analysis of the temporal cross-correlations also permits an evaluation of the relationships between the SSB input parameters (SWH, WS, and MWP), where distinct behaviors are found in the swell- and wind-sea-dominated areas, and associated time scales are less than or on the order of 1 day. Finally, it is demonstrated that computing cross-correlations between the SLA (with and without SSB correction) and the SSB input parameters offers an additional tool for evaluating the relevance of candidate SSB input parameters, as well as for assessing the performance of SSB correction models, which, so far, mainly rely on the reduction in the variance of the differences in the SLA at crossover points.

Keywords: ocean altimetry; sea state bias; SWOT; sea-state variability; decorrelation time scales; temporal cross-correlations

Citation: Mazaleyrat, E.; Tran, N.; Amarouche, L.; Vandemark, D.; Feng, H.; Dibarboure, G.; Bignalet-Cazalet, F. Analysis of High-Frequency Sea-State Variability Using SWOT Nadir Measurements and Application to Altimeter Sea State Bias Modelling. *Remote Sens.* **2024**, *16*, 4361. https://doi.org/10.3390/rs16234361

Academic Editor: Xianwei Wang

Received: 2 October 2024
Revised: 14 November 2024
Accepted: 16 November 2024
Published: 22 November 2024

1. Introduction

Satellite altimetry has evolved to become the primary means for global observations of sea surface height (SSH) and long-term monitoring of the sea surface height anomaly (SSHA). The latter, also referred to as the sea level anomaly (SLA), corresponds to the SSH minus the reference mean sea surface [1,2]. Satellite altimetry also measures the significant wave height (SWH) data, which, at the moment, is the only parameter characterizing

surface waves that is measured globally and on a continuous basis. Additionally, satellite altimetry measures the ocean surface backscattering coefficient, from which near-surface wind speed (WS) can be derived using empirical algorithms [3–5]. In order to obtain centimetric precision in the SSH, the raw radar-measured distance to the surface (i.e., the range) must be corrected for atmospheric propagation delays and several distinct surface geophysical effects. Among the latter, the sea state bias (SSB) correction adjusts the range measurement to compensate for known errors due to the presence of waves on the ocean surface. Left uncorrected, altimetric sea level would lie below the true sea level. This correction is commonly applied using empirically derived two-dimensional (2D) SSB models involving two of the previously mentioned altimeter-derived measurements, namely, SWH and WS [6–10].

The present altimeter constellation provides along-track measurements that are sparse in time and space. Thus, interpolating SSH gridding algorithms are routinely applied to merge multi-mission datasets, using an optimal interpolation routine requiring several pre-processing steps and covariance characterization [11–13]. The European Union's Earth observation program, Copernicus, currently provides daily sea level maps and their along-track sources with accuracy achieving 1–4 cm rms [14] through the Copernicus Marine Service (CMEMS). These long records for SSH and SLA are extremely useful for studying mesoscale eddies, large-scale ocean circulation variability, and sea level rise [15–17], and they now cover the last three decades. Still, only the largest ocean mesoscale features can be presently resolved [18–20] due to the effective spatio-temporal resolutions of the altimetry gridded products (O(100 km) and O(10 days), respectively). These resolutions are not adequate for capturing all processes acting at the sea surface, and they are especially limiting in regions with energetic baroclinic turbulence. Such regions experience rapid changes in smaller-scale SSH anomalies at time scales well below that of the shortest satellite altimeter repeat orbit sampling periods (i.e., 10 days for altimetry reference missions) [21].

Operational constraints on mission orbit selection do not typically allow simultaneous high spatial resolution and high temporal resolution. However, the newly launched (16 December 2022) Surface Water Ocean Topography (SWOT) altimeter offers several new opportunities to observe ocean variability at enhanced temporal and spatial resolutions. Indeed, as of 26 July 2023, SWOT has settled into its main orbit (referred to as SWOT science orbit) characterized by a 21-day revisit period, and its new interferometric altimeter offers unprecedented spatial resolutions, potentially resolving 15–30 km wavelengths [22,23]. Moreover, during its early flying phase (referred to as the SWOT fast-sampling phase), which lasted from 29 March to 11 July 2023, the SWOT satellite followed a 1-day repeat orbit used for sensor calibration and validation. This unique orbit, characterized by very sparse ground tracks, allowed for observation of rapidly moving small-scale ocean SLA signals [23–25]. And it is expected that measurements from this specific phase can also improve our general knowledge on the high-frequency variability (i.e., 1–10-day time scales) in wind and sea-related parameters.

In the present study, SLA, SWH, and WS data are retrieved using SWOT's on-board conventional nadir radar altimeter rather than the SWOT innovative primary payload, which consists in the Ka-band radar interferometer (KaRIn). The SWH and WS measurements provided by nadir altimeters are in close agreement with in situ data, with accuracies in the 10–40 cm range for SWH [26,27], as summarized by Woo and Park [28], and lower than 1.5 m/s for WS [3,29–31]. Mean wave period (MWP) data are also included in the present study, since MWP (combined with SWH and WS) can be used to provide alternative three-dimensional (3D) SSB solutions to better describe SSB behavior and efficiently remove the sea-state's impact on raw altimeter range measurements [32,33]. Both the standard 2D SSB model (which relies on SWH and WS) and the 3D SSB model are available in GDR-F reprocessed products for Jason-2/3 and AltiKa missions and are provided in SWOT nadir products since launch. In the present study, MWP data are retrieved using ERA-5, a numerical global ocean wave model.

The present paper provides an analysis of the short time-scale (<10-day) variability of metocean parameters obtained using SWOT nadir altimeter measurements from the fast-sampling phase, followed by a discussion on the implications for SSB modelling. The unique 1-day repeat observations are of interest because the high-frequency dynamics of SWH, WS, and SLA time series are difficult to observe over large ocean basins. Instead, they were previously only observed at specific locations using buoys, deep ocean moorings, and/or tide gauges.

The objectives of the present study are threefold, as follows: (i) to quantify and analyze the decorrelation time scales associated with the three input SSB model descriptors (SWH, WS, and MWP) and the spatial variations in these time scales; (ii) to examine the temporal cross-correlations among SSB descriptors, as well as between SLA and SSB descriptors, to gain further insight into the relationships connecting all considered parameters; and (iii) to use study findings to reconsider standard assumptions and approaches used in empirical SSB modelling.

Standard techniques associated with time series analysis are applied, namely, the use of autocorrelation functions (ACFs) and cross-correlation functions (CCFs). The present paper is organized as follows. The considered datasets are described in Section 2 along with the SSB modelling approach and key methodological aspects related to ACFs and CCFs. The results are then presented in Section 3. Finally, Section 4 is devoted to implications of said results for SSB modelling, as well as perspectives for future work.

2. Data, Corrections, and Methods

2.1. SWOT Nadir Altimeter Combined with ERA-5 Model

The SWOT mission, launched on 16 December 2022, carries two different radar altimeters. Its primary and innovative instrument, KaRIn, is not the focus of the present study. Although KaRIn aims to measure ocean surface topography with unprecedented spatial resolution and accuracy, its retrieval of both SWH and WS parameters is not yet mature (as of the time of the present study) compared to the second SWOT system—the Poseidon-3C nadir altimeter. The latter is a Jason-class dual-frequency (Ku/C) altimeter that ensures continuity of data records and consistency in the measurement technique with its predecessors for meteorology, operational oceanography, and climate applications. In addition to differences in the altimetry technology with KaRIn, the Jason-class nadir altimeter points straight down and collects data in one dimension while the two KaRIn antennas cover a two-dimensional surface swath of over 120 km wide, with a +/−10 km gap about the nadir, collecting SLA data with greater precision than the nadir altimeter alone [34].

SWOT surveys the globe in a near-circular, non-sun-synchronous orbit at an altitude of 890 km and an orbital inclination of 77.6°. Because of the swath coverage, the number of repeat observations at a given location during its nominal 21-day science orbit varies with latitude, from two repeats at the Equator to four at the mid-latitudes to more than six at the high latitudes [35]. This rather coarse temporal sampling does not allow for the study of small-scale rapid ocean processes, the time scales of which are comparable to or shorter than the sampling intervals. To satisfy scientific research team requests to resolve these processes, SWOT spent about six months in the 1-day fast-sampling phase. The first 3.5 months of said orbit were used for engineering checkout and to calibrate the instrument parameters. The second period (29 March–10 July 2023) was dedicated to scientific data collection and studies [24]. The data analyzed in the present study were extracted from this latter period.

The altimeter-based dataset of the present study included 1 Hz altimeter measurements extracted from the SWOT Level 2 Nadir Altimeter Interim Geophysical Data Record (IGDR) Version 1.0 dataset available at AVISO (Archiving, Validation, and Interpretation of Satellite Oceanographic data) [36]. The nadir along-track measurements have a spatial sampling of approximately 6 km at 1 Hz. The spatial coverage associated with SWOT fast-sampling phase is sparse; it comprises only 28 passes, with ~1430 km (resp. 2860 km) between

adjacent orbital ascending and descending nodes (resp., between adjacent orbital ascending nodes) at the Equator [24].

Contrary to SLA measurements, the altimeter-derived records for the SWH (denoted hereafter as SWH_alti) and WS (WS_alti) provided in the aforementioned dataset are directly used as such. Note that the data used in the present study originates from the processing of radar echo waveforms with an MLE4 retracking algorithm [37,38], which is the standard method used to generate the long Jason data records. The following four parameters were retrieved using MLE4: range, SWH, backscatter coefficient (sigma0), and the antenna mispointing angle. Sigma0 (together with SWH) was used to infer the wind speed with the Jason-1-based model [4], while the range was used within the SLA computation.

Regarding the SLA data exploited in the present study, estimates from the IGDR reprocessed dataset are not directly used as such. Instead, the SLA values are updated using the latest recommended barotropic corrections for SWOT [39] while keeping all other range corrections unaltered. These updates concerned both the global tidal model and the dynamical atmospheric correction (DAC) applied to generate a highly accurate SLA. The FES2022C tidal model has an improved bathymetry and a globally enhanced high-resolution mesh, which leads to significant improvements for both tidal elevations and currents compared to the FES2014B version available for current SWOT products. For the DAC, a specific version dedicated to the SWOT 1-day fast-sampling phase was used. It better removes high-frequency ocean signals forced by atmosphere pressure at this temporal sampling rate. The updated DAC consists of a 2-day filtered DAC, while the operational DAC corresponds to a 20-day filtered DAC adapted to 10-day repeat orbits (details are available on AVISO [40]). Finally, different versions of the SLA are analyzed depending on the applied SSB corrections, and they are presented in Section 2.2.

Regarding the model estimates of the atmospheric wind- and sea-state parameters, neither the ECMWF model wind estimates nor the MF-WAM wave model mean zero-crossing wave periods (T_{02}) (which are available in the IGDR products) were used because of inconsistencies between the model parametrizations. Instead, both the WS and MWP estimates, denoted here as WS_model and MWP_model, are taken from the ERA-5 dataset [41], as well as a modelled SWH (SWH_model). ERA-5 is the most recent global reanalysis dataset produced by ECMWF. It is the successor of the ERA-Interim and provides hourly reanalysis data from 1950 to present. The full dataset is available from the Copernicus Climate Data Store with a pre-interpolated resolution of up to $0.25^\circ \times 0.25^\circ$ for atmospheric parameters and $0.5^\circ \times 0.5^\circ$ for wave parameters. The model data used in the present study are interpolated onto SWOT nadir ground track locations using a bilinear interpolation in space and a linear interpolation in time. Note that SWH data from some altimeters (namely, ERS-1/2, ENVISAT, JASON-1/2, CRYOSAT-2, and SARAL) are assimilated into the ERA-5 reanalysis using an optimal interpolation scheme, but SWOT is not one of them. ERA-5 data can, therefore, be considered here as independent. Finally, for SWOT altimeter data quality control, the in-house screening process from cal/val activities was applied to remove all questionable measurements.

2.2. SSB Correction

A detailed review of ocean altimeter range measurement methods, including the impacts due to the sea state range correction, can be found in Chelton et al. (2001) [1]. Briefly, the net SSB is predominantly made up of the electromagnetic range bias, which stems from smoother wave troughs reflecting more radiant energy than rougher wave crests [42]. This electromagnetic bias leads to a discrepancy between the desired mean sea surface and the measured lower mean reflecting surface. Next, most altimetric range retrackers are designed to locate the mid-power point of the leading edge of the radar time return signal. This equates to measuring the median reflecting surface, rather than the mean. The median reflecting surface is again lower than the mean reflecting surface because of the known non-Gaussian distribution of surface heights over the illuminated footprint,

leading to a skewness bias. Finally, SSB accounts for a final third effect, historically referred to as the tracker bias, which combines contributions from each instrument's design, the signal processing, and the SSH's computation [1,2]. These three effects (which must be considered to satisfy the current altimetry needs) are difficult to isolate and describe within a single consistent additive physical model, while empirical models simply estimate a net SSB effect. Consequently, the SSB correction remains a relatively uncertain range error term.

The SSB estimation approach used by most authors consists of building empirical models based on the satellite altimeter data itself [7–9,33,43,44]. SSB is, therefore, a singular correction among all other range corrections in ocean altimetry. In essence, because there is no observable SSB, it is extracted from SSH data (uncorrected for SSB), and then a range adjustment is modelled using parametric [6,45] or nonparametric methods [7,8,33,43,44,46] which depend on independent sea state measurements or estimates.

SSB was originally simply modeled as a percentage of the SWH with a coefficient in the range of 2–5% [47], forming so-called one-dimensional (1D) SSB models, and then expressed as a function of both the SWH and WS in 2D models. Two-dimensional models are now commonly used to correct the range in operational SLA products. More recently, the use of the mean wave period as a third predictor in 3D models shows some success in improving the sea-state-related range bias description [32,33,48–50]. The wave period provides information on wave steepness associated with the degree of the wave's nonlinearity [51], while the local WS provides information on the wind-generated small-wave roughness contributing to the electromagnetic bias via hydrodynamic modulation [52,53].

While SWH remains the main driver of the SSB description, the improvement gained with 2D and 3D models points to the incompleteness of the SWH alone in describing the SSB variability with the required accuracy, as well as the need for additional measures linked to the wave field variability and nonlinearity.

The following three sets of SSB models are used in the present study and four SLA estimations are considered: an SLA version uncorrected for SSB, denoted as SLA_uncorr, and three SLA estimations for which the 1D, 2D, and 3D SSB models are, respectively, applied and denoted as SLA_corr1D, SLA_corr2D (i.e., "standard" SLA), and SLA_corr3D. The three SSB solutions are determined by Collecte Localisation Satellites (CLS) based on the latest Jason-3 GDR-F version data. The 1D (BM1) model corresponds to −3.2% SWH. As for the 2D and 3D SSB corrections, they are provided in GDR-F products for MLE4-based SLA computation [54]. They are built based on a nonparametric approach called the local linear kernel smoothing statistical technique, developed by Gaspar et al. [8], and later improved by Tran et al. [9,33]. This approach has been used to develop all SSB models in the form of 2D and 3D grids used for the Jason altimeter missions.

The main difficulty in empirical SSB determination lies in the extraction of sea-state-related signals in SSH data, since the latter contains both oceanographic signals and undesired signals, such as orbit errors, residual errors from geophysical and environmental corrections, and instrumental noise. In order to cancel out these errors (or at least limit their leakage into the SSB model because of artificial geographical correlations between such SSH residual errors and the sea-state descriptors), SSB models have traditionally been estimated using time-differenced SSH at specific locations along the satellite track [6]. Depending on the mission's characteristics, these differences can be computed from a collinear analysis of repeat cycles or from satellite pass crossovers. For Jason-like missions with a repeat cycle of ~10 days, SSB models are based on collinear differences, while missions with a higher repeat cycle are built using crossover differences [46,55]. The differencing eliminates the time-invariant constituents, i.e., the geoid signal and the steady part of dynamic ocean topography. In both cases, the SLA (uncorrected for SSB) differences can be written as follows:

$$\mathrm{SLA\_uncorr}_2 - \mathrm{SLA\_uncorr}_1 = (\mathrm{SSB}_2 - \mathrm{SSB}_1) + \varepsilon$$

where the subscripts 1 and 2 distinguish data obtained at the same geographical location but at the following two different times: t_1 and t_2; ε is assumed to be a zero-mean error term

that includes all altimetric measurement errors but not SSB, plus the dynamic topography variation between t_1 and t_2. Note that the time difference $t_2 - t_1$ is restricted to 10 days, a duration in which the slower large-scale ocean circulation is assumed to remain relatively constant, a result which has recently been questioned by Dibarboure and Morrow [21]. But assuming this, the non-zero value of the SLA difference is, therefore, attributed to the SSB, while contributions from other constituents are neglected [6]. Minimization procedures are then used to express the SSB in terms of the considered sea-state descriptors (depending on the considered model's dimensions). Such model computation effectively reduces the overall variance in the SLA differences, and this is interpreted as an effective removal of SSB impacts.

In the nonparametric approach, minimization consists in solving a large linear system of equations in which the SSB is the unknown parameter [8] to determine cycle-based 2D or 3D grids. To account for seasonal changes in sea-state conditions, a sufficient amount of individual cycle-based models must be considered that cover at least a 1-year period. These models are then averaged to obtain the annual version. Additionally, to remove the small contamination of the SSB model by the dynamic topography variation within 10 days (rather than neglect it as it was previously done) [6], two intermediate annual solutions are in fact computed. While the first one uses sea-state descriptors at t_2 for computing the relationship between SSB and its correlatives, the second one uses those observed at t_1. Lastly, the final model corresponds to the mean value of the two grid tables, as explained in Tran et al. [9].

SSB models developed with collinear or crossover datasets are identical from a methodological point of view, but the advantage of a collinear dataset (over a crossover one) lies in the abundance of data samples. At each cycle, ~450,000 samples for the former vs. ~7000 samples for the latter are available to feed the system of equations used to compute the individual SSB models, which directly influences the robustness of the empirical models. In practice, not all available data is used because inverting such a matrix would require a prohibitive amount of computation time. For instance, in Gaspar et al. (1998) [7], 500 crossover points were randomly extracted for each cycle. In Gaspar et al. (2002), the use of the least squares QR (LSQR) decomposition method [56] greatly reduced the computation time, and all ~7000 valid crossover samples per cycle were used. Jiang et al. [50] mentioned the use of 8000 samples when using a similar nonparametric approach but with the least squares minimum-residual method (LSMR) [57], which further reduced the computation time by 10–15% compared with the LSQR. For the Jason SSB models, CLS uses ~15,000 randomly selected collinear pairs to keep the computational burden reasonable. As a result, only 3% of the data per cycle is used, and this selection can include redundant information. Because the WS, SWH, and MWP are cross-correlated parameters, a trade-off among three aspects should be found, as follows: (1) keeping a reasonable matrix size while maintaining a large enough dataset to provide stable statistics, (2) avoiding redundancy by selecting optimal independent sea-state correlatives and (3) limiting as much as possible the impact of residual oceanic variability in the SSB computation process. All three aspects need to be addressed to guarantee the robustness of SSB empirical models.

In the present study, the examination of the decorrelation time scales of SWH, WS and MWP along with the analysis of their cross-correlations should help in building optimal SSB training datasets. The selection of thinned datasets will likely remain compulsory, especially when considering wide-swath altimeters such as KaRIn. During SWOT 21-day science phase, ~40 M individual crossover points are generated per cycle, with a significant amount of redundant information. This could overwhelm computation time needs for the SSB model estimation. The present paper also further discusses the relationships between the SSB correlatives and the SLA, and investigates their dependencies at short time scale.

2.3. Construction of SWOT Time Series

Time series, each associated with a specific location and presenting 1-day sampling, were constructed through projection and linear interpolation of updated or unaltered (see

Section 2.1) 1 Hz Level 2 SWOT nadir altimeter IGDR products onto a reference ground track. The considered period covers an approximately 3.5-month period during the SWOT fast-sampling phase, from 29 March to 10 July 2023, which corresponds to SWOT cycles 474 to 578. 105-day-long time series were constructed for nine parameters, namely, SWH_alti, SWH_model, WS_alti, WS_model, MWP_model, SLA_uncorr, SLA_corr1D, SLA_corr2D, and SLA_corr3D. SLA_corr1D and SLA_corr3D were not further processed, as they were not used for computing ACFs and CCFs. In contrast, for the seven other parameters, only the time series presenting more than 60 valid values (out of the available 105) were included in the present analysis. Linear interpolation was performed to fill in the remaining missing data. Out of the ~55,000 locations over the ocean included in the 28 passes of the SWOT fast-sampling phase, ~20% of the locations were associated with "invalid" time series (i.e., those having fewer than 60 valid values), leaving a "valid" dataset of ~44,000 locations.

2.4. Autocorrelations and Cross-Correlation Computations

Estimating the decorrelation time scale (DT) of a parameter provides useful insight into its temporal variability. Large (resp., low) DT express slow (resp., fast) temporal changes and are associated with persistent (resp., ephemeral) phenomena. Most DT estimation methods rely on autocorrelation functions (ACFs). ACFs measure the correlation (i.e., similarity) of a temporal series, X, with a delayed copy of itself as a function of the delay (i.e., time lag), k. They are, therefore, well-suited for analyzing the temporal persistence of a process. Other possible DT estimation methods rely on power spectral density [58,59], detrended fluctuation analysis [58,60], or ordinal pattern probabilities [61]. In the present study, an ACF-based approach was used, where the ACF of a time series, X, is defined as follows:

$$ACF(X,k) = \frac{\sigma_{xx}(k)}{\sigma_{xx}(0)}$$

with $\sigma_{xx}(k) = \frac{1}{n}\sum_{t=1}^{n-k}(x_{t+k} - \overline{x})(x_t - \overline{x})$, where $\overline{X}$ is the mean value of the time series X, and n is the number of samples in the X series. ACFs are independent of the initial time point and, thus, only depend on the time lag, k. They are characterized by a maximal initial value of 1 at lag 0 and then decrease with increasing time lag, k. The time scale over which an autocorrelation function tapers is related to the decorrelation processes at hand, which, for geophysical parameters, can depend both on external forcing and local dynamics.

Note that DT estimation depends heavily on the sampling interval and time duration of the selected time series. The sampling interval should be sufficiently small (typically, less than half of the actual DT, for Nyquist-related reasons [62–64]) and the time duration sufficiently long (typically 20 to 50 times the actual DT [63–65]) to provide a reliable DT estimate.

Several ACF-based definitions for DT can be found in the literature. The zero-crossing and half-crossing are the most widespread definitions; they assign the DT to the time delay associated with the first ACF zero-crossing (resp., the first ACF 0.5 crossing) and are denoted as L_0 (resp., L_{half}) [66]. Because these definitions are very sensitive to long-range correlations, which tend to produce slowly decaying ACFs, integral scales have been introduced, as follows: L_1 and L_2 are defined as the discrete integrals of the ACF and squared ACF, respectively [66–70]. Other decorrelation scale definitions, based on Gaussian or exponential decay fits, require some a priori knowledge on the data generation process. A detailed comparison among the L_0, L_{half}, L_1, and L_2 estimations is provided in Appendix A, along with the rationale supporting our choice of using L_2 estimates in the present study.

Cross-correlations between the selected parameters are examined in the present study using cross-correlation functions (CCFs). The latter measure the correlation (or similarity)

of a temporal series, X_1, with a delayed copy of a temporal series, X_2, as a function of the delay, k, using the following formula:

$$CCF(X_1, X_2, k) = \frac{\sigma_{x_1 x_2}(k)}{\sigma_{x_1} \times \sigma_{x_2}}$$

where $\sigma_{x_1 x_2}(k) = \frac{1}{n} \sum_{t=1}^{n-k} (x_{1\,t+k} - \overline{x_1})(x_{2t} - \overline{x_2})$, $\overline{x_1}$ (respectively, $\overline{x_2}$) is the mean value of the temporal series X_1 (respectively, X_2); σ_{x_1} (respectively, σ_{x_2}) is the standard deviation associated with the temporal series X_1 (respectively, X_2); and n is the number of samples in the X_1 and X_2 series. To avoid spurious correlations caused by autocorrelations in the original time series and/or shared trends, a prewhitening procedure is applied [71]. This procedure is standard in cross-correlations analysis. It allows for the identification of meaningful relationships between the pairs of series (X_1 and X_2) (i.e., between the selected parameters).

Prewhitening was applied to each and every considered pair of series (X_1 and X_2) and consisted of (1) fitting an autoregressive integrated moving average ARIMA(p, d, q) model to the original X_2 time series; (2) retrieving the associated X_2 residuals; and (3) filtering the X_1 original time series using the previously determined X_2 ARIMA(p, d, q) model parameters. Note that p and q are the orders associated, respectively, with the autoregressive (AR) and moving average (MA) terms, while d is the differencing order associated with the integrated (I) part. Cross-correlations were then computed between the X_2 residuals and filtered X_1 to identify the potential time-lagged correlations. The $(p,\ d,\ q)$ orders of the X_2 models were selected using the Akaike information criterion [72], ensuring a trade-off between the goodness of fit and the simplicity of the model. The ARIMA models' identifications were undertaken using the *auto_arima* function from Python package (pmdarima version 2.0.4).

3. Results and Discussions

3.1. Mean and Variance of SLA Differences with Respect to Time Lags

The SWOT 1-day sampling phase offers an unprecedented opportunity to precisely assess assumptions used for SSB modelling, as well as to more accurately quantify and compare the performances of the three available SSB corrections (1D, 2D, and 3D models). Figure 1 summarizes these results. They are computed using the following four versions of SLA time series: SLA_uncorr, SLA_corr1D, SLA_corr2D, and SLA_corr3D. For the first time, statistical indicators derived from SLA differences are computed based on a 1-day repeat orbit dataset covering all ocean surfaces, with time intervals between SLA observations ranging from 1 day to up to 50 days. The changes in SLA occurring for time intervals below 10 days are especially interesting to evaluate both the current model assumptions and performance. Note that, contrary to what is usually done at CLS, the models' performances are evaluated here using SLA variance reduction measurements based on collinear differences rather than differences at crossover points.

The computation of the statistical indicators of interest was performed as follows. First, four datasets of SLA time series were built, each associated with a certain SLA version (identified with the respective suffixes "uncorr", "1D", "2D", and "3D"). Then, within each dataset, groups of SLA differences (DSLA) were extracted, each associated with a fixed time interval equal to 1 day, 2 days, . . ., up to 50 days. This step led to a total of 50 subsets per SLA version. Prior to computing the global statistical indicators (namely, the mean and variance of each subset), two random selections were performed to ensure that all subsets relied on the same number of SLA pairs. Indeed, in the absence of any particular selection, subsets associated with smaller time intervals are naturally more populated than those associated with larger time intervals. Statistics computed from such uneven datasets could be affected by sampling biases. The two selections involved extracting, respectively, 1,981,813 and 15,000 SLA pairs per subset. The former size ensures the largest possible

dataset, while the latter corresponds to a size commonly used by CLS for cyclic SSB model estimations.

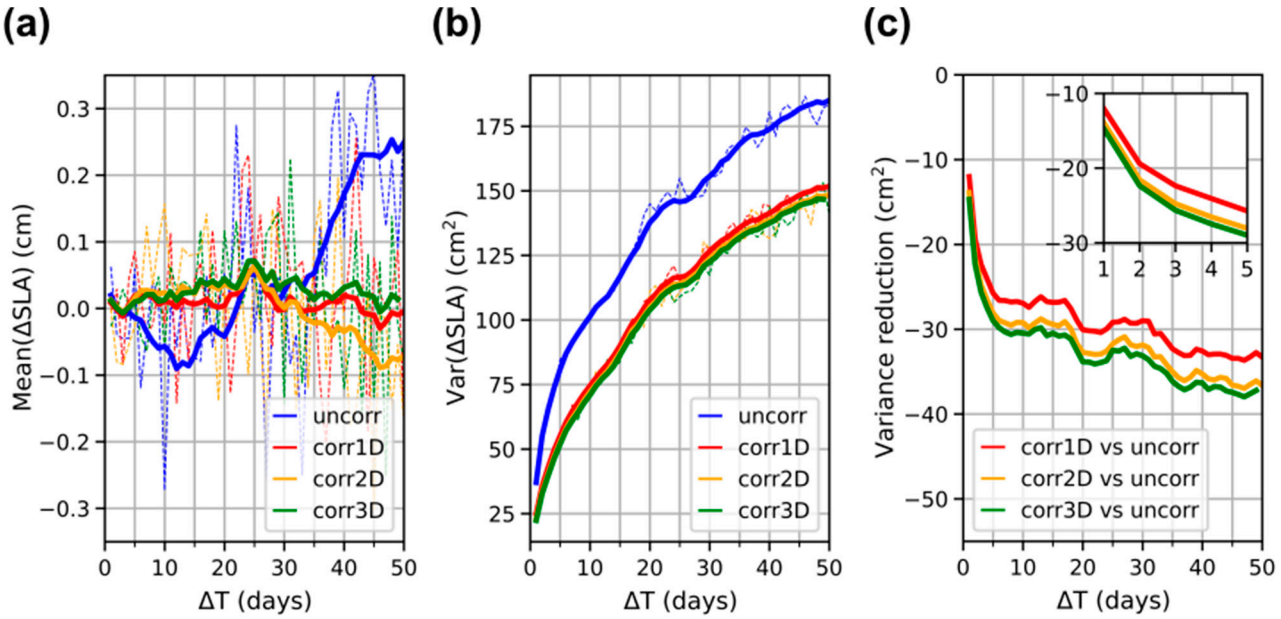

Figure 1. (**a**) Global means of the SWOT nadir SLA collinear differences as a function of the time interval considered for the SLA differences. The examined SLA types are SLA_uncorr (no SSB applied), SLA_corr1D (application of SSB = −3.2% SWH), SLA_corr2D (with J3 GDR-F 2D SSB table), and SLA_corr3D (with J3 GDR-F 3D SSB table); (**b**) same as in (**a**) but for the global variance; (**c**) global variance reduction as a function of the considered time interval obtained when one computes var(ΔSLA_corr) minus var(ΔSLA_uncorr). Negative values indicate an improvement in the SLA precision resulting from the application of the SSB correction. Higher reduction magnitudes indicate greater model skill.

The global mean and variance values associated with each subset are reported in Figure 1a,b, respectively, as a function of the time interval. The results associated with the four versions of the SLA are displayed with thick solid lines for the ~2 M-large selection and thin dotted lines for the 15,000-large selection. For time intervals below 10 days, the mean differences associated with DSLA_uncorr were lower than 1 mm (resp., 3 mm) for the ~2 M-large (resp., 15,000-large) selection (Figure 1a). These results corroborate the general assumption stating that ε can be considered as a zero-mean error term (cf. Section 2.2). Note, however, that this assertion stands for a global estimation of ε, when all sea-state conditions are covered. Because SSB computation is performed locally in the descriptors' space, it can be verified that in sparsely populated regions, ε values do not verify the zero-mean assumption. In practice, this characteristic entails that two SSB solutions per cycle are computed (which are then averaged), as described in Section 2.2. Finally, note that after SLA was corrected, the mean differences remained below 1 mm (for the ~2 M-large selection), whatever the considered SSB correction, and for time intervals as large as 50 days. This confirms the consistency in both the SLA content and precision provided by the SSB correction.

As expected, the global variance in DSLA increases with the time interval (Figure 1b). This is due to the increase in the contribution of the rapid mesoscale changes associated with western boundary currents, internal waves and tides, the development of sub-mesoscale fronts, filaments and small-scale eddies, the displacement of larger eddies, meanders, planetary waves, etc. [21]. The global variance is expected to increase up to a final plateau, at which a maximum is reached. Such a plateau is not observed here, presumably due to the 50-day limitation. The variance in the DSLA is also lower when SLA is corrected for SSB, and it is increasingly lower when the SSB dimension increases, confirming that more

SSB error is removed when additional descriptors are considered. This feature is more clearly observed in Figure 1c, which presents the reductions in the variances obtained when comparing uncorrected SLA differences with (1D, 2D, and 3D) corrected SLA differences. Contrary to Figure 1a,b, Figure 1c only displays the results associated with the ~2 M-large selection. A reduction in said diagnostic (i.e., negative values) indicates an improvement in the internal consistency of SLA data, thus a more accurate estimate of SLA. Indeed, the higher the reduction, the better the model, since a reduction in variance is interpreted as variance explained by the applied SSB model [9,32,46,73].

Note that when the time interval is at its minimum value (1 day), the computed variances in Figure 1b are low (~37 cm² for DSLA_uncorr and ~22–25 cm² for DSLA_corr) yet non-zero, as they comprise both the 1 Hz altimeter noise and the 1-day rapid ocean variability (as well as some residual SSB errors). As is evident from Figure 1c, the reduction in variance increases within the first five days and then reaches an initial plateau between ~5 and 15 days. After the first 5 days, the relative improvement in the performance could roughly be considered as stable for all three SSB versions. The presence of two distinct behaviors before and after 5 days points to a disparity in the contributions to the reduction in variance before *versus* after 5 days. Such differences could be related to the notion of dependent/independent observations through temporal persistence and/or temporal cross-correlations. While temporal persistence designates the presence of correlations between two observations of a given variable separated by a certain time delay, temporal cross-correlations refer to the presence of correlations between the observations of two different variables taken either at the same time or separated by a certain time delay. If the temporal persistence of a specific SSB descriptor is long, two observations of such a descriptor separated by a short time interval cannot be considered as independent. Likewise, if two SSB descriptors present cross-correlations—*a fortiori* time-lagged cross-correlations—then, the two SSB descriptors cannot be considered independent. In the present case, it is likely that, if one or both types of correlations exist, they are associated with time scales on the order of a few days. The analysis of such correlations and the potential implications for SSB modelling have not been investigated so far. The fast-sampling SWOT nadir dataset provides a unique opportunity to address these points using satellite- and model-based data. The temporal decorrelation scales of the SSB descriptors are analyzed in Section 3.2, while the temporal cross-correlations among the SSB descriptors are examined in Section 3.3. Finally, the temporal cross-correlations between the SLA and SSB descriptors are reported in Section 3.4. Such analyses should help tentatively explain the two distinct features observed for the variance reductions, namely, a rapid increase (in absolute values) from 0 to 5 days and the subsequent overall stabilization between 5 and 15 days. It should also provide insight into whether the cross-correlations among the SSB descriptors should be of concern for SSB modelling. Should the observed correlations be removed in some way? Should SSB modelling approaches be revised?

3.2. Temporal Decorrelation Scales for SWH, WS, and MWP

The present section reports on results associated with the DT for each of the five SSB input-related parameters under study, namely, SWH_alti, SWH_model, WS_alti, WS_model, and MWP_model. As previously mentioned in Section 2.4, DTs were estimated based on ACF, using L_2 definition (see Appendix A). In principle, ACFs (and, therefore, ACF-based DT estimates) are only defined for stationary time series. Therefore, prior to computing ACFs and DT, the stationary/non-stationary character of the selected time series was assessed. The main sources of time series non-stationarity include (1) the presence of a deterministic trend, (2) seasonal effects (associated with constant periods, typically 1 year), and (3) unit roots. In the present study, the presence of a deterministic trend was ruled out through visual inspection of the time series and the absence of any *a priori* argument in favor of a deterministic trend. Second, the analyzed SWOT 3.5-month time period (29 March to 10 July 2023) is too short to account for seasonal effects. Finally, the presence of a unit root was tested using the most common method, namely, the augmented Dickey–Fuller (ADF)

test [74,75]. The ADF results are summarized in Table 1. The ADF test was conducted using all of the time series of all selected input parameters, and the results were compared to a significance level of 5%; if the p-value is less than 0.05, the ADF null hypothesis stating the presence of a unit root is rejected; therefore, the time series is considered stationary. Otherwise, the null hypothesis cannot be rejected, implying non-stationarity.

Table 1. Percentages of the time series classified as stationary/non-stationary for the five considered SSB input-related parameters, according to the ADF test run with a 5% significance level.

	Are the Considered Time Series Stationary?	
	Yes	**No**
SWH_alti	87.3%	12.7%
SWH_model	83.2%	16.8%
WS_alti	90.0%	10.0%
WS_model	89.8%	10.2%
MWP_model	90.4%	9.6%

Table 1 provides the percentages of the time series among the valid dataset categorized as stationary (and, therefore, associated with a so-called differencing order $d = 0$)/non-stationary ($d = 1$). A vast majority (~80–90%) of the time series are stationary for all five SSB input-related parameters. It is likely that those classified as non-stationary are, in fact, stationary long-memory time series associated with $0 < d < 0.5$. This is because the ADF test has low power in distinguishing such series from unit roots since it only considers $d = 0$ and $d = 1$ hypotheses. Moreover, long-range correlations (typical of stationary long-memory time series) have been identified in both wind speed [60,76] and significant wave height records [58,59,61], while fractional-ARIMA models (which allow for long-memory time series to be explicitly modeled) were used to forecast wind speed data [76,77]. To assure the long-memory stationary character of the ~10–20% "ADF-non-stationary" time series, the fractional differencing order d should verify $0 < d < 0.5$. Unfortunately, the low number of samples per time series (i.e., 105 here) prevents any reliable estimation of the fractional differencing order d using methods such as the Geweke and Porter-Hudak's and the Sperio's estimation methods [78,79].

Hereafter, it is therefore assumed that the stationary character and, thus, the ACF-based DT computation also hold for the minority of "ADF-non-stationary" time series. Moreover, the integral DT scales used in the present study are well-suited for time series exhibiting long-range correlations. Note that a published ACF-based analysis on wind speed data [80] relied on a similar stationarity assumption.

Figure 2 shows examples of the ACFs of time series taken at two different locations from SWOT nadir pass 28 (locations are shown in Figure 2a). The time series were selected among the two altimeter-derived parameters (SWH_alti and WS_alti) and the three model-based estimates (SWH_model, WS_model, and MWP_model). Although each time series is 105-day-long, the ACFs are displayed with 0- to 20-day time delays (Figure 2b,c), as most of the ACF tapering occurs within the first few days. The selected parameters (SWH, WS, and MWP) can, in principle, vary at different time scales, with the largest variations often observed at seasonal scales. However, as mentioned before, the study time series are too short to account for seasonal effects. The horizontal dashed black lines in Figure 2b,c indicate the 95% significance confidence interval, which serves to assess the significance of the correlation values. Any correlation value that falls outside (resp., within) the 95% confidence interval is considered significant (resp., not significant, as it may not be differentiated from random correlations). After 10 days, it is clear that all five parameters are no longer autocorrelated at both locations.

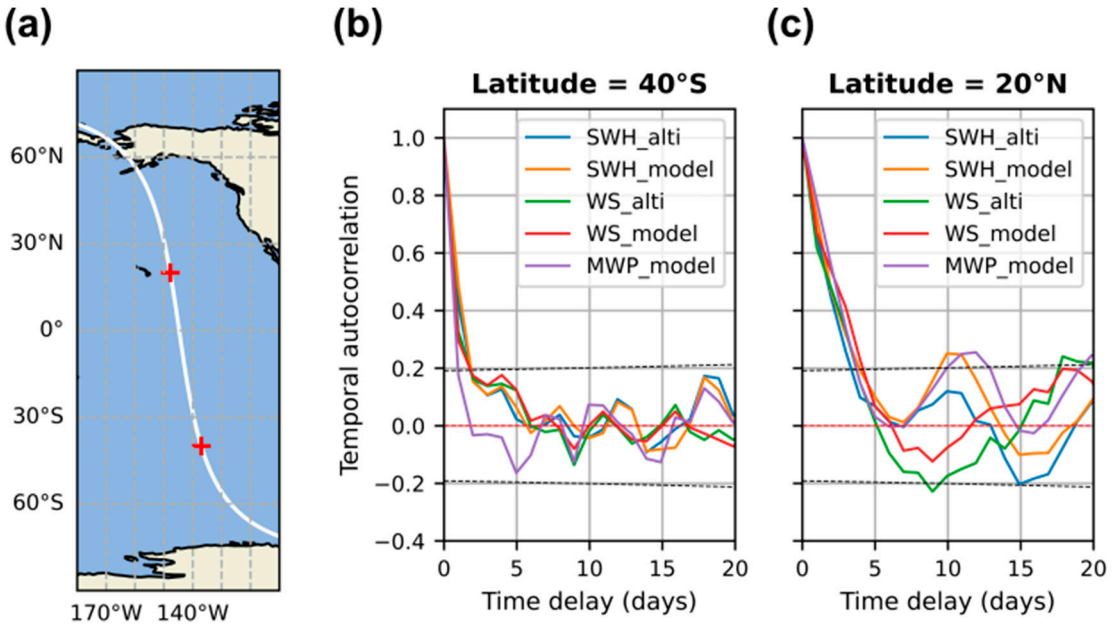

Figure 2. (**a**) Map showing the two locations from SWOT nadir pass 28 (40°S and 20°N) associated with the ACFs shown in (**b**,**c**); (**b**) autocorrelation functions (with associated 95% confidence intervals as dotted lines) of the five considered SSB input-related parameters at the 40°S location; (**c**) same as in (**b**) but for the 20°N location.

The ACF of the surface WS is, perhaps, the easiest to grasp (among the three sea-state descriptors), as it provides direct insight into the time scales governing wind variability. The determination of such time scales allows for the wind variability to be characterized as "fast" or "slow" relative to other components of the climate system. They are also useful for characterizing the WS statistical predictability, as they provide a measure of wind persistence [60,76,77]. The ACFs of the SWH and MWP are, perhaps, more difficult to comprehend, since both parameters are controlled by two wave categories with different characteristics: wind waves and swell. The former are locally generated short-wavelength waves with more chaotic characters, and they travel less rapidly than the surface wind. They are strongly wind-forced and are affected by factors such as wind duration, fetch, and speed. In contrast, swells are usually generated remotely by storms or prevailing winds, such as trade or westerly winds, which blow over long fetches and long durations [81–83]. They are long-wavelength waves with a smoother appearance and can propagate thousands of kilometers across the ocean without extracting energy from wind and with little energy loss [51,84,85]. Numerous studies [83,86–91] indicate that, in most ocean basins, the sea state is a mixed superimposition of local wind seas and at least one swell system; the latter originating from a remote region and propagating in a direction different from the local wind. Factors influencing wind/wave field variability are, thus, intricate; while wind-sea variations reflect short-scale wind changes, the swell variability reflects wind changes over an extended spatio-temporal domain.

For a more global view of the ACF structure of the selected parameters, one can display ACF maps at specific time delays rather than plot the ACFs as a function of the time delay at a few specific locations. By doing so, it is found that the geographical distribution of the ACF structure associated with WS_alti is in good agreement with results published by Monahan [80]. Monahan provided maps of the wind speed ACFs at +1 day, +2 days, and +3 days, derived from scatterometry SeaWinds data (see Figure 1, right panel, in that study). Similar to the present study, Monahan assumed stationarity for the surface vector winds. Regions that present an autocorrelation value that remains close to 1 after 3 days (such as the Arabian Sea, in red in both Figure 1, right, in ref. [80] and Figure A3 in Appendix B of the present study) have long DTs, while the high latitudes show rapidly

decreasing autocorrelation values (from yellow at +1 day to green at +3 days in both of the aforementioned figures).

Now turning to the ACF-based DT computations, global maps of the DT estimates are provided in Figure 3 for SWH_alti (Figure 3a), WS_alti (Figure 3b), and MWP_model (Figure 3c). Because of the spatial coverage associated with the SWOT fast-sampling phase, the displayed results are evidently scarce. For all three parameters, most DTs range from 1 to 4 days, with minimal values (<2 days) associated with the mid-latitude regions in the Southern Hemisphere (between 30°S and 60°S) or located beyond 60°N/S. Maximal values (up to 10–14 days) are uncommon but found in different areas depending on the considered parameter (namely, the Arabian Sea for SWH and WS, the North Atlantic Ocean for SWH and MWP, and the mid-latitude Pacific Ocean for all three parameters). The particularly high DT levels for wind speed observed in the Arabian Sea are attributed to the steady southwesterly wind speeds occurring in that region during the June–September southwest monsoon [92–94]. Overall, the DTs associated with SWH_alti are larger than those associated with the other two sea-state descriptors, and the mean and median DT values for the former parameter amount to ~2.5 days and ~2.1 days, respectively, while the ones associated with the latter two parameters are lower, at ~2.1 days and ~1.8 days, respectively. Finally, the distributions of the DT values in days (illustrated by the histograms in Figure 3) are more similar and skewed for both WS and MWP than the larger and more even DT distribution associated with SWH.

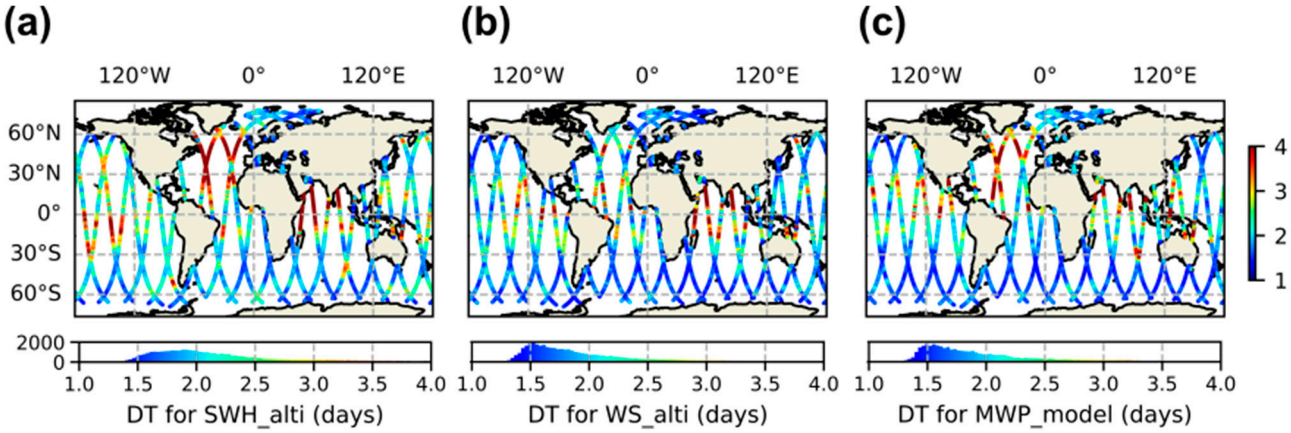

Figure 3. Maps of the decorrelation time scales: (**a**) SWH_alti; (**b**) WS_alti; (**c**) MWP_model.

To make further sense of the spatial DT variations, the dependence of the DT values on the mean metocean conditions is analyzed. For each time series, the mean metocean values (mean SWH_alti, mean WS_alti, and mean MWP_model) and the computed DTs are associated. Figure 4 presents 2D binned plots of the DTs of SWH_alti as functions of the (mean SWH, mean WS) (Figure 4d), (mean SWH, mean MWP) (Figure 4e), and (mean MWP, mean WS) (Figure 4f). The associated density plots are shown in Figure 4a–c. Overall, Figure 4 suggests that the SWH_alti DTs can be roughly divided into two subsets: regions of high wind and rough sea-state conditions (WS > 9 m/s, SWH > 3 m, and MWP > 6.5 s) are associated with low DT values (<2 days), while regions with more moderate conditions (WS < 9 m/s, 1 m < SWH < 3 m, and MWP < 6.5 s) display larger DT values (> 2 days). Note that the DTs of WS_alti and MWP_model show similar dependence on the mean metocean conditions. The overall finding is relatively intuitive: high wind and rough sea areas (which are more subject to phenomena that can disrupt temporal correlations) present less persistent wind/wave states than moderate wind/wave regions. A refined interpretation of the precise DT geographical variations is next presented based on an analysis of the metocean processes at play.

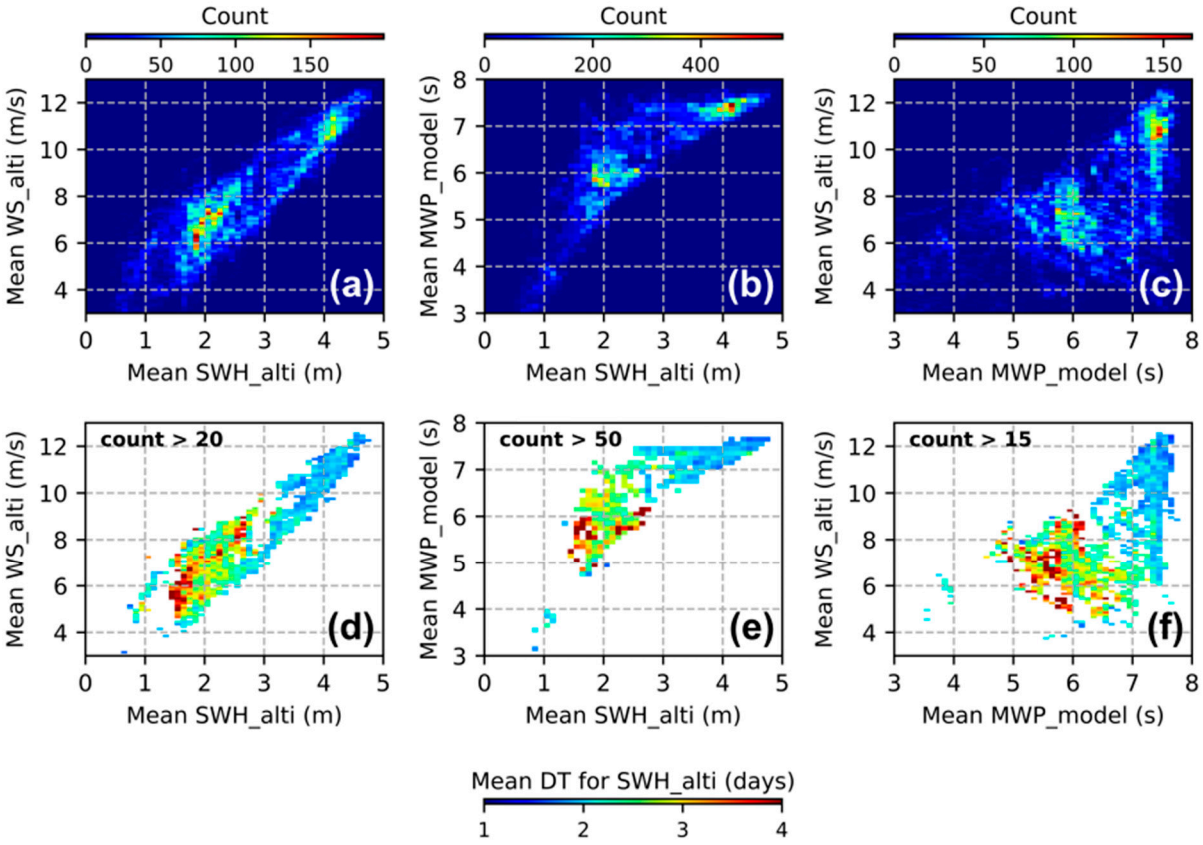

Figure 4. Decorrelation time scales of SWH_alti with respect to the mean sea-state conditions covered by the SWOT fast-sampling nadir dataset: (**a**–**c**) density plots of the decorrelation time scales with respect to (**a**) (mean SWH_alti and mean WS_alti); (**b**) (mean_SWH_alti and mean MWP_model); (**c**) (mean MWP_model and mean WS_alti). The 3D space associated with the mean sea-state conditions (SWH, WS, and MWP) was binned, and the number of occurrences (i.e., count) pertaining to a specific bin is color-coded. (**d**–**f**) Same as in (**a**–**c**), except the decorrelation time scale values (rather than the number of their occurrences) are color-coded.

The sparse spatial coverage associated with the SWOT fast-sampling phase naturally limits the full exploitation of the geographical patterns observed in Figure 3. But since the Earth's large-scale atmospheric circulation is organized around dominant zonal wind belts, the average latitudinal variations in DT (with their associated standard deviations) are computed, using 3° latitudinal bands. In addition to the three parameters already reported in Figure 3 (SWH_alti, WS_alti, and MWP_model), the latitudinal DT variations of SWH_model and WS_model are included, and all five zonal statistics are provided in Figure 5. An overall DT latitude-dependency is clear and common for all three SSB descriptors; latitudes between 30°S and 60°S and beyond 60°N/S are associated with low (<2 days) average DT values and very low dispersions (<1 day), while the tropical areas present higher (>2 days) average DT values and very large dispersions (up to 5 days). It is also found that the altimeter-based and model-based estimates are in close agreement for SWH and WS in their essential features. This finding is consistent with the overall agreement found between altimeter-based and model-based DT estimates shown in Appendix A.

In an attempt to ascribe the DT latitudinal variations observed in Figure 5 to metocean processes, the mean wind/wave latitudinal variations are shown in Figure 6 (with their associated standard deviations). In agreement with previous observations, the DT variations are anticorrelated with the mean wind/wave variations (rough winds and sea-state conditions are associated with low DTs, while moderate conditions present higher DTs). The latitudinal variations reported in Figure 6 are consistent with general knowledge of global atmospheric circulation and seasonal metocean conditions. Despite the Earth's

atmospheric circulation varying from year to year, its large-scale structure remains fairly constant over time and is characterized by several zonally oriented strong or weak prevailing wind patterns with systematic recurrences of local wind regimes. From the Equator moving poleward, these wind patterns include the calm-wind doldrums within ± 10°; the tropical Easterlies, or trade winds, located between 10° and 30°; the Westerlies, with the strongest features peaking at around 50°; and the Polar Easterlies beyond 60°.

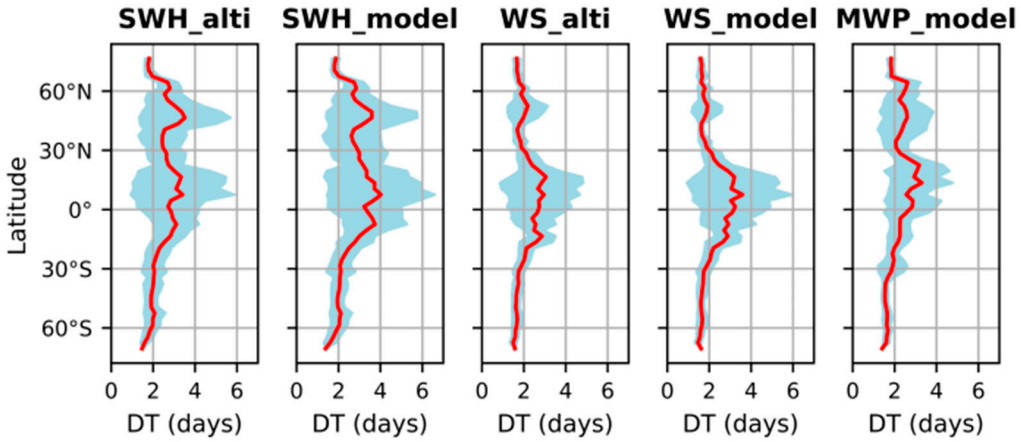

Figure 5. Average latitudinal variations (in red) and associated dispersions (in blue) of the decorrelation time scales of the five considered SSB input-related parameters. The zonal averages were computed using 3° latitudinal bands, and the displayed dispersions correspond to ± one standard deviation.

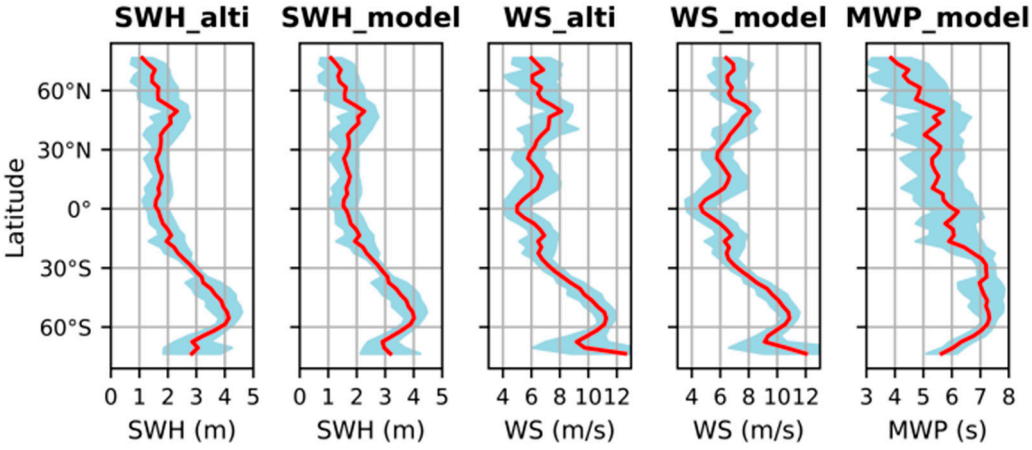

Figure 6. Average latitudinal variations (in red) and associated dispersions (in blue) of the mean values of the five considered SSB input-related parameters. The zonal averages were computed using 3° latitudinal bands, and the displayed dispersions correspond to ± one standard deviation.

The average wind/wave distributions vary from one season to the next and are characterized by an asymmetrical phase opposition between the two hemispheres; the intensity of the wind and sea-state conditions is weaker in the Northern Hemisphere than in the Southern Hemisphere at corresponding latitudes, but presents a larger WS seasonal variability. Within the period considered here (end of March to mid-July), a clear Southern Hemisphere dominance is observed, especially in the extratropics (Figure 6). The highest wind and wave conditions, peaking at respectively ~11 m/s and ~4 m, occur at the mid-latitudes between 30°S and 70°S (Figure 6), with the onset of the intense storm activities characterizing the austral winter. These storm activities will reach their maximum intensity in July–August, a few weeks after our observation window. Secondary maxima at ~8 m/s for WS and ~2.4 m for SWH are observed at mid-latitudes in the Northern

Hemisphere (Figure 6). Both the global and secondary wind/wave maxima are associated with storm patterns of the Westerlies (in their respective hemispheres), where small-scale weather systems (e.g., mid-latitude depressions and passage of atmospheric fronts), or extra-tropical/polar cyclones occur chaotically. At most latitudes, maximal WS values occur when the considered hemisphere experiences winter, while minimal ones occur in the summer. In the Northern Hemisphere, peak conditions occur during boreal winter (January) in both the North Pacific and North Atlantic Oceans. Considering the observation period at hand, the secondary maxima in WS and SWH are attributed to the decreasing seasonal activities of the Westerlies in the North Pacific and North Atlantic. The decrease starts in March and is expected to reach a minimum in July/August. These Westerlies blow from West to East, and steer extra-tropical cyclones in this general direction. They generate the local wind waves forming the circumpolar wind sea belt in the Southern Ocean. As for the extensive northwest gales originating from the main continents at mid-latitudes during boreal winter, they are the primary cause of the seasonal wind-wave generation in the Northern Hemisphere. Ebuchi et al. [95] reported for instance that strong winds blowing constantly from Siberia toward the west coast of Japan usually last longer than a day, hence generate numerous wind-wave events in the Sea of Japan. The Westerlies in the Southern Hemisphere are more consistent throughout the year and more intense as they find no interruption by land in the East–West direction. It is often assumed that the associated high wave conditions are a result of the extended fetch. Young [96] rather pointed out that the high wind speeds and the duration of the storms are more important factors. Finally, Zhang et al. [97] highlighted that not only the highest SWH are all situated in the Westerlies of the Southern Hemisphere, but MWP also displays a maximum value in this particular region. Said MWP maximum amounts to ~7.3 s in the present dataset (Figure 6); wave periods are greater since waves have time to build up and generate longer swells. As can be seen from Figure 6, the higher consistency of the Westerlies in the Southern Hemisphere results in lower wind/wave latitudinal dispersions compared with the Northern Hemisphere.

During the observation period associated with the present study, the major wind-sea-dominated regions are the extratropical storm areas and the Southern Westerlies regions [83,88]. Such regions are associated with highly correlated WS and sea-state parameters (Figure 6). On the contrary, in swell-dominated areas (roughly $\pm 25^{\circ}$), the wind and wave fields display fewer similarities (Figure 6).

Three well-defined tongue-shaped zones of swell dominance, commonly referred to as "swell pools", are located in the eastern tropical areas of the Pacific, Atlantic, and Indian Oceans. The west coast of the Americas is notably influenced by long period swells originating from both hemispheres, while the swell zone in the Atlantic Ocean is associated with shorter periods compared with the Pacific and Indian Oceans [96]. Swell generated in the Southern Ocean has a particularly significant impact on much of the world's oceans. Although it mainly propagates from west to east, part of it propagates for large distances away from the area in which it was generated and penetrates the adjacent Pacific, Atlantic, and Indian Ocean basins. However, because of the narrower geometry of the Atlantic Ocean, swells generated in the Southern Ocean do not appear to influence wave conditions all the way up to the North Atlantic [96].

WS, SWH, and MWP show an overall progressive decrease from the Southern high latitudes to the Equator, but only WS presents a local maximum in the subtropical region (Figure 6). This local maximum is associated with the trade-wind belts and is absent from both wave fields as they are less coupled with wind in swell-dominated areas. More precisely, swells coming from the Southern Ocean have larger heights and longer periods than local wind waves and, therefore, "mask" the locally trade-wind generated events. The net result is that SWH and MWP fields vary far more smoothly than WS does. In contrast with the high latitudes, the equatorial area is associated with low SWH (Figure 6). In this region, the swell energy weight is almost permanently close to 100% [83,86,87,89,98,99] since swells originating from both the Northern and Southern high latitudes commonly

reach the equatorial region. The area is also dominated by the doldrums and their associated low WS fields.

In light of the wind and wave conditions occurring during the 3.5-month observing period, the DT geographical distributions associated with the SSB descriptors (Figures 3 and 5) can be better interpreted. A direct correspondence between the DT values of WS, which mostly range from 1 to 4 days, and the locally active weather systems (organized around dominant zonal wind belts) can be drawn. Note that storms that are too short-lived or diurnal variations are not accounted for in the present dataset. DT values associated with the WS in the Southern Hemisphere Westerlies are slightly lower than those observed in the Northern Hemisphere Westerlies, and they exhibit a stronger spatial homogeneity (Figures 3b and 5), consistent with the overall homogeneity of the Southern Hemisphere Westerlies wind belt. The DT values of WS in this region mirror the rapid displacement of relatively strong events, the regularity of their passage at fixed locations and their low seasonal variability. In contrast, in the Northern Hemisphere, the DT features associated with the WS are reminiscent of weaker, hence, more irregular events associated with slower dynamics and a larger variety in the types of events. In trade winds areas, the prevailing winds give rise to weak/moderate, hence, irregular meteorological events resulting in larger DT values and greater spatial variability (Figures 3b and 5). In contrast with the tropical Pacific and Atlantic Oceans, the large DT values observed in the Northern Indian Ocean (Figure 3b) are ascribed to the unique two-season weather pattern characteristic of the southwest monsoon, which, during the observed period, results in steady southwesterly wind speeds [92–94].

Now turning to the DT distributions associated with wave fields (Figures 3a,c and 5), their large similarities with the ones associated with WS (Figures 3b and 5), especially south of 30°N, evidence the significant influence of WS over SWH and MWP through atmospheric forcing. Still, large DT disparities between wind and wave fields are observed in some regions. For instance, the North Atlantic Ocean exhibits wave field conditions associated with significantly higher persistence than wind (Figure 3). These disparities suggest that SWH variability is partly controlled by swell variability, which can itself have little similarity with the local wind pattern [100–102]. The results presented here also agree with a study limited to the Norwegian Sea, which showed that, statistically, the persistence of wave fields decreases with increasing wave height [103]. Examples from this study include wave fields with SWH > 12 m and lasting only a few hours and those with SWH > 3 m and lasting up to 8 days. Finally, a large anomaly occurring in spring 2023 in the North Atlantic Ocean climate [104] might explain the differences observed between the Atlantic and Pacific Oceans in the DTs of the wave fields (Figure 3a,c). Irregular rapid ocean warming in the eastern equatorial basin from March to June associated with unusual stagnant and weaker-than-average surface winds throughout the east and central Atlantic were observed and indicated the onset of an Atlantic Niño event [105,106]. This unusual weakening of both the mid-latitude westerly flow and the tropical–subtropical easterly trade winds in the Atlantic Ocean compared with the Pacific area may have had a minor impact on wind DTs (Figure 3b) and a significant one on the wave field DTs (Figure 3a,c), provided that the swell energy contribution is different in the two basins.

In summary, presented satellite-based results are in close agreement with numerical models and are largely consistent with expected global wind/wave systems distributions and their interactions. High-latitude rough seas have less wind/wave persistent characteristics because they are wind-coupled areas characterized by strong and variable winds. By contrast, regions with weak/moderate wind fields are swell-dominated areas, characterized by low SWH and a larger swell variability, resulting in longer-lasting features with higher DT dispersion ranges.

3.3. Cross-Correlations Between SWH, WS, and MWP

Most of the metocean variables examined in the present study are correlated, to some extent, through relationships that may not always be instantaneous. Swells generated

remotely by storms may take several days to reach a given location and influence the local dynamics. Considering time-lagged cross-correlations might, thus, be useful to better grasp the mixed wind/sea influences at a particular location and to identify potential regionally varying behaviors. The analysis conducted next surely has limitations, since wind seas and swells were not considered separately. Still, examining the cross-correlations among the sea-state descriptors may help future SSB modelling efforts related to (i) estimating region-specific SSB models or (ii) accounting for the observed correlations within an adapted SSB estimation approach.

As mentioned in Section 2.4, a prewhitening procedure was applied to each considered pair of series $(X_1,\ X_2)$ prior to computing the cross-correlations. The cross-correlations were then computed between the X_2 residuals and X_1 filtered series. Note that, as expected, similar results were obtained when (X_2 residuals, X_1 filtered) or (X_1 residuals, X_2 filtered) series were used to compute $(X_1,\ X_2)$ cross-correlations. In addition, only the cross-correlations associated with successful prewhitening were analyzed; the Ljung–Box test [107], set with a significance level of 5%, was used to determine whether the X_2 residuals were autocorrelated. X_2 residuals failing the Ljung-Box test were excluded from the analysis; they represent only 2.4% to 4.1% of the entire valid dataset depending on the selected X_2 parameter.

For each $(X_1,\ X_2)$ combination, the cross-correlation values associated with positive time delays relate the similarity between the non-delayed X_1 series and the X_2 series delayed with a positive lag. In other words, the correlations associated with positive time delays inform whether X_1 is a predictor of X_2, whereas the correlations at negative lags indicate whether X_2 is a predictor of X_1. Be aware that the presence of correlations between two parameters does not necessarily imply causality; for instance, a third parameter might be needed to explain the observed correlations. Hereafter, the correlations among SWH, WS, and MWP are analyzed through the computation of the following three cross-correlations combinations: (WS_alti, SWH_alti), (SWH_alti, MWP_model), and (WS_alti, MWP_model).

Figure 7 presents examples of the CCFs computed at the two locations from SWOT nadir pass 28 shown in Figure 2a. The horizontal dashed black lines in Figure 7 indicate the 95% significance confidence interval. Similarly to the ACF case, it was computed as $\pm\frac{1.96}{\sqrt{n-k}}$, where n is the total number of observations and k is the lag. In the present case, the confidence interval amounts to approximately $\pm$ 0.2 in the time delay range of interest (between $-$10 days and +10 days). Most of the significant cross-correlations (i.e., the cross-correlation values falling outside the confidence interval) occur at lags 0 and +1 day, as shown in Figure 7. For instance, significant positive correlations associated with (WS_alti, SWH_alti) combination are observed at lags 0 and +1 day on both selected locations of pass 28. For the 40°S location (Figure 7a), a large (WS, SWH) correlation (i.e., 0.46) was observed at lag 0 and a moderate one (0.30) at lag +1 day, meaning that increased WS is associated with higher SWH both immediately and, to a lesser extent, 1 day after the increase in WS. This finding is attributed to atmospheric forcing. After 1 day, the correlation rapidly decays and becomes non-significant. (SWH_alti, MWP_model) combination presents relatively similar features, i.e., significant positive correlations at lags 0 and +1 day at both locations, while (WS_alti, MWP_model) only showed significant correlations at 40°S, with a negative (rather than positive) correlation at lag 0 and a positive correlation at lag +1 day.

The presence of significant correlations at lags 0 and +1 day is confirmed at the global scale for all three combinations as summarized in Table 2, where the percentages of locations exhibiting significant (positive or negative) correlations at lags $-$2 days, $-$1 day, 0 day, +1 day, and +2 days are provided for all three combinations. Large percentages (>72%) of significant correlations at lag 0 and moderate percentages (between ~36% and 46%) at lag +1 day are found for the three combinations. The other three time delays presented in Table 2 (namely, $-$2 days, $-$1 day, and +2 days) are associated with low (<10%) percentages. In a nutshell, WS can be seen as a short-term (up to +1 day) predictor of both SWH and MWP, while SWH is a short-term (up to +1 day) predictor of MWP. Again, note that the predictive character of SWH on MWP does not necessarily imply causality; it is likely that

SWH and MWP present correlations due to a third-party influencing variable rather than through a direct causal relationship.

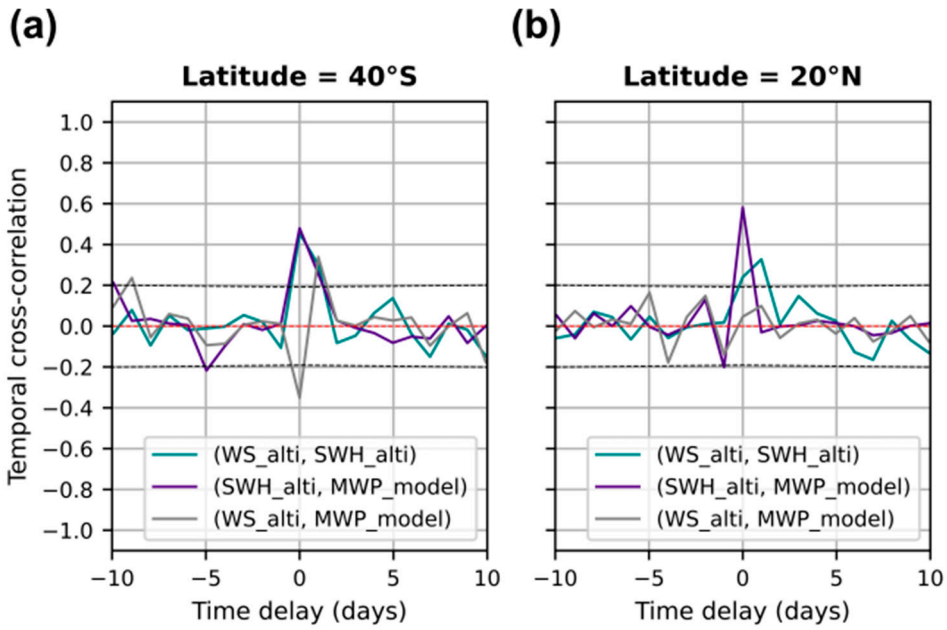

Figure 7. Cross-correlation functions (with the associated 95% confidence intervals as dotted lines) of the three considered SSB input-related parameters combinations at the (**a**) 40°S and (**b**) 20°N locations from SWOT nadir pass 28, as shown in Figure 2a. For each of the three (X_1, X_2) combinations, the correlations associated with positive time delays inform on whether X_1 is a predictor of X_2, whereas the correlations at negative lags indicate whether X_2 is a predictor of X_1.

Table 2. Percentages of locations associated with significant correlations (i.e., falling outside the 95% confidence interval) for the three considered SSB input-related parameters combinations at lags of −2 days, −1 day, 0 day, +1 day, and +2 days. Percentages above 10% are highlighted in bold.

	−2 Days	−1 Day	0 Day	+1 Day	+2 Days
(WS_alti, SWH_alti)	3.4%	8.2%	**88.1%**	**36.5%**	5.4%
(SWH_alti, MWP_model)	4.6%	7.9%	**89.7%**	**43.5%**	5.1%
(WS_alti, MWP_model)	3.4%	6.8%	**72.7%**	**45.7%**	7.8%

The cross-correlation maps associated with lags 0 and +1 day for the three selected combinations are presented in Figure 8. They unveil, for each considered time delay and combination, the geographical variations in the cross-correlation values. For clarity reasons, the non-significant correlations (excluded by means of the 95% confidence interval) were removed from all maps, leaving an empty [−0.2, 0.2] range. Overall, the maps associated with lag 0 (Figure 8a–c) present a vast majority of significant correlations (>72% according to Table 2), hence, do not exhibit large gaps ("missing" points) in correlation values. The 0-lag correlations are also mostly positive for (WS_alti, SWH_alti) (Figure 8a) and (SWH_alti, MWP_model) (Figure 8b), and mostly negative for (WS_alti, MWP_model) (Figure 8c), and they all exhibit a clear latitudinal dependency.

For (WS_alti, SWH_alti) combination (Figure 8a), the highest correlation values (from 0.5 to 0.75) are observed in wind-sea areas like the Westerlies. In such regions, SWH is mainly composed of wind-wave height, which itself directly depends on wind strength and duration. As a result, SWH variability is directly governed by variations in the local atmospheric conditions. In contrast, moderate correlations (from 0.2 to 0.5) are found in swell-dominated tropical areas, where the local WS and total SWH variations are less coupled.

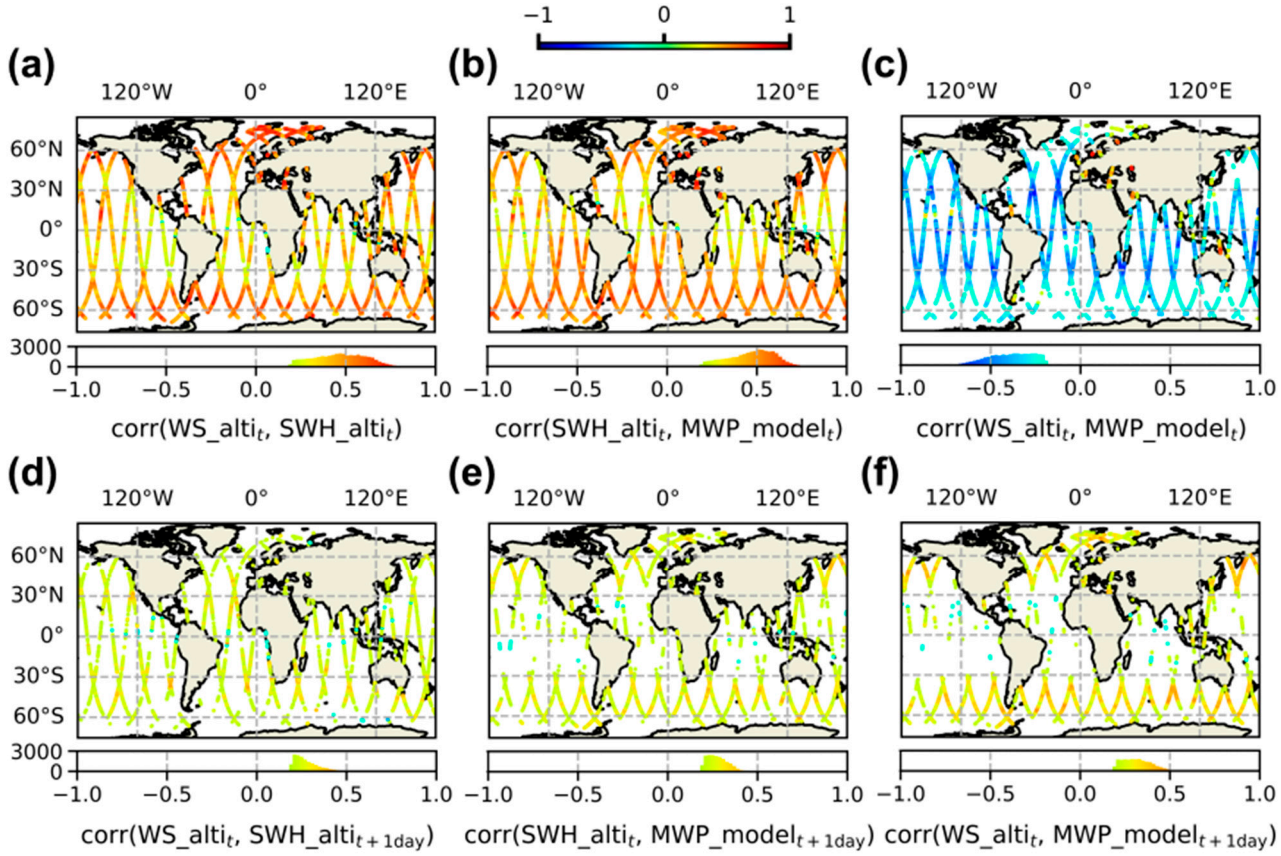

Figure 8. Maps of cross-correlation values for the three SSB input-related combinations mentioned in Table 2 at time delays equal to (**a**–**c**) 0 day and (**d**–**f**) +1 day. Non-significant correlations (i.e., falling within the 95% confidence interval) were removed from all maps, leaving an empty [−0.2, 0.2] range.

Regarding (SWH_alti, MWP_model) combination (Figure 8b), features similar to the ones associated with the 0-lag (WS_alti, SWH_alti) map are observed; the highest correlation values (from 0.5 to 0.75) occur at mid-latitudes as well as along relatively long segments equatorward, while moderate correlations (from 0.2 to 0.5) are found in swell-dominated areas. Increases in SWH values are, therefore, associated with simultaneous increases in the MWP values, especially in wind-sea-dominated regions. The relationship connecting SWH and MWP is not straightforward as they are spectral parameters influenced by swell and wind-sea contributions. A fixed wave height can be associated with a wide range of periods. This is evident from scatter diagrams presented by Haselsteiner et al. [108] in their attempt to construct contours on joint distributions. More precisely, Haselsteiner et al. showed that for a SWH value equal to 1 m, the wave period varies from roughly 2 s to 13 s, while for a 4 m-high wave it ranges from 6 s to 11 s. Still, the results shown here are in good agreement with the statistical modelling presented in [108], which shows that an increasing wave steepness (i.e., height/wavelength) is associated with joint increases in SWH and MWP values.

As for (WS_alti, MWP_model) combination (Figure 8c), its associated 0-lag map differs from the maps of the two previous combinations; large negative cross-correlation values are found in tropical regions, while weaker negative correlations and/or non-significant correlations ("missing" points) are observed at mid-latitudes. Finally, a minority of regions exhibit positive (WS, MWP) correlations. These are mostly closed seas regions including the Mediterranean, North, Baltic, Black and Caspian Seas and the Persian Gulf in Europe and Asia, the Caribbean Sea in America and the Arafura Sea in Oceania. The dominance of negative correlations is, at first sight, in apparent contradiction with the other two 0-lag maps; how can MWP be negatively correlated with WS and positively

correlated with SWH, while SWH is itself positively correlated with WS? In fact, the regions that exhibit the highest positive (WS, SWH) correlations (such as the high latitude regions in red in Figure 8a) are associated with non-significant or positive (WS, MWP) correlations (high latitude regions lacking points or in yellow/green in Figure 8c). Overall, the relationship between WS and MWP depends on a complex spectral distribution of wave components. In regions of intense wave growth such as the mid-latitudes, the wave spectrum depends on a variety of waves, from ripples to swells. These waves evolve rapidly through the continuous transfer of energy from wind to surface waves and nonlinear wave-to-wave interactions, as well as other transformative processes such as white capping and wave dispersion (related to swell propagation to other regions). The associated rapid evolution of the wave spectrum (and, therefore, of MWP estimates) is difficult to relate to a WS change as the latter sets off a cascading process. Different attempts to statistically describe (WS, MWP) relationship in regions of intense wave growth have been published in the literature [109,110]. Regarding now swell-dominated regions, the high (WS, MWP) observed correlation values are indicative of a simpler relationship, where increasing winds are almost systematically followed by an "immediate" decrease in MWP. In such regions, wind-sea and swell contributions to the wave spectrum are more distinctly separated; wave spectra typically display bi-modal features where an intense low-frequency primary peak is associated with swell components while a moderate high-frequency secondary peak is related to wind waves. As wind speed increases, a transfer of energy from the atmosphere to the high-frequency part of the spectrum occurs. This energy transfer is associated with capillary wave generation and wave-to-wave interactions, which result in the formation of a larger family of gravity-capillary waves, inducing a shift of the average wave energy toward higher frequencies, thus a decrease of MWP. Note that T_{02} definition (used for MWP in the present study) is more dependent on the high-frequency components than other wave period definitions [111–113], resulting (in swell-dominated areas) in a clear (WS, MWP) relationship, as follows: increasing WS values are associated with decreasing MWP estimates.

Now turning to the +1 day-lag maps (Figure 8d–f), the ones associated with the first two combinations (Figure 8d,e) show weaker significant positive correlations (around 0.25) compared with their corresponding 0-lag maps, especially in the mid-latitudes. Regarding (WS, SWH) combination (Figure 8d), the observed correlations are again attributed to atmospheric forcing; although the +1 day-delayed response of waves is less widespread and less intense than the immediate (0 day) response, increased wind speeds on a specific day tend to result in higher waves on the day after. (WS, SWH) correlation gaps (associated with non-significant correlations) are preferentially observed around the Equator, where calm winds lead to very weak atmospheric forcing. Overall, SWH variability is predominantly influenced by swell variability rather than wind variability. As for the third (WS_alti, MWP_model) combination (Figure 8f), the +1 day-lag map mostly presents significant correlations of opposite sign (i.e., positive) compared with the 0-lag map. These are also limited to the mid-latitudes. The change in sign from the 0 day-lag to the +1 day-lag map is indicative of the overall unobvious relationship between WS and MWP.

In summary, the analysis of the temporal cross-correlations among the SSB descriptors follows known metocean relationships [114–116]. The present study, which relies on newly available altimetry and model-based data, is largely consistent with previous analyses, which were essentially model-based [83,91,108,117,118] or derived from buoys measurements [119,120].

3.4. Cross-Correlations Between SLA and SSB Descriptors

The last aspect covered in the present paper is an analysis of the cross-correlations between SLA and SSB descriptors. For this particular study, the selected SLA time series are restricted to SLA_uncorr and SLA_corr2D, as the latter is the standard version provided to altimetry users. The following six cross-correlations combinations were examined:

(SWH_alti, SLA_uncorr), (WS_alti, SLA_uncorr), (MWP_model, SLA_uncorr), (SWH_alti, SLA_corr2D), (WS_alti, SLA_corr2D), and (MWP_model, SLA_corr2D).

Table 3 presents, for each combination, the percentage of significant cross-correlations at lags −2 days, −1 day, 0 day, +1 day, and +2 days, while Figure 9 displays the cross-correlation maps at 0-lag associated with the different combinations. Again, non-significant correlations (excluded by means of the 95% confidence interval) were removed from all maps, leaving an empty [−0.2, 0.2] range. As expected, for all considered combinations, the highest percentages of significant correlations are found at lag 0, meaning that the correlations between SLA and SSB descriptors are mostly immediate. The significant correlations observed at other lags (close to lag 0) are ascribed to inertia in the coupled atmosphere–ocean system. The largest percentage of significant cross-correlation values at lag 0 is observed for (SWH_alti, SLA_uncorr) combination (98.4% in Table 3) and is associated with the average largest absolute cross-correlation value (see the histogram in Figure 9a), both elements confirming that SWH is the main driver of the SSB. SWH is followed by WS and then MWP as the SSB descriptors, since the latter two exhibit increasingly smaller percentages of correlations (82.5% and 32.8% in Table 3) and increasingly smaller average absolute cross-correlation values (see the histograms in Figure 9b,c). Unsurprisingly, the cross-correlations are negative for (SWH_alti, SLA_uncorr) combination, which is related to the negative value of the SSB correction.

Table 3. Percentages of locations associated with significant correlations (i.e., falling outside the 95% confidence interval) for the six considered (SSB input-related parameter, SLA) combinations at lags −2 days, −1 day, 0 day, +1 day, and +2 days. Percentages above 10% are highlighted in bold.

	−2 Days	**−1 Day**	**0 Day**	**+1 Day**	**+2 Days**
(SWH_alti, SLA_uncorr)	6.2%	9.9%	**98.4%**	7.6%	6.2%
(SWH_alti, SLA_corr2D)	6.1%	**10.9%**	**31.8%**	**10.7%**	7.9%
(WS_alti, SLA_uncorr)	6.0%	**11.6%**	**82.5%**	**23.1%**	8.0%
(WS_alti, SLA_corr2D)	5.9%	7.3%	**23.4%**	**10.2%**	7.4%
(MWP_model, SLA_uncorr)	4.9%	**22.6%**	**32.8%**	**12.0%**	6.1%
(MWP_model, SLA_corr2D)	5.4%	**10.2%**	**22.0%**	8.5%	6.7%

As expected, adjusting SLA measurements using the 2D SSB correction model results in drops in both (i) the fraction of locations associated with significant cross-correlations (Table 2: from 98.4% to 31.8% for (SWH, SLA); 82.5% to 23.4% for (WS, SLA); and 32.8% to 22.0% for (MWP, SLA)) and (ii) the absolute average cross-correlation values (Figure 9a,d, Figure 9b,e, and Figure 9c,f: from −0.56 to −0.23 for (SWH, SLA); −0.40 to −0.12 for (WS, SLA); and −0.24 to 0.11 for (MWP, SLA), respectively). These drops indicate that the SSB correction successfully removes or weakens most of the existing correlations between SLA and SSB descriptors. Note that despite the MWP not being explicitly included in the 2D SSB correction, this correction still removes or weakens part of the existing correlations between SLA and MWP. This finding is likely attributed to the co-variability of the three SSB descriptors reported in Section 3.3: correcting SLA using SWH and WS indirectly corrects SLA for some of the MWP-related bias. For a proper evaluation of the ability of an SSB model to remove (MWP, SLA) correlations, SLA_corr3D (rather than SLA_corr2D) should be exploited. Finally, even after correcting SLA with the 2D SSB correction, a small dependency on the latitude remains (Figure 9), with larger cross-correlation values observed at the mid- and high-latitudes. The weaker yet persisting latitude-dependent correlations between sla_corr2D and the three SSB descriptors indicate that the applied SSB correction is perfectible. Deriving an SSB solution directly from SWOT nadir data is likely to improve the results presented here.

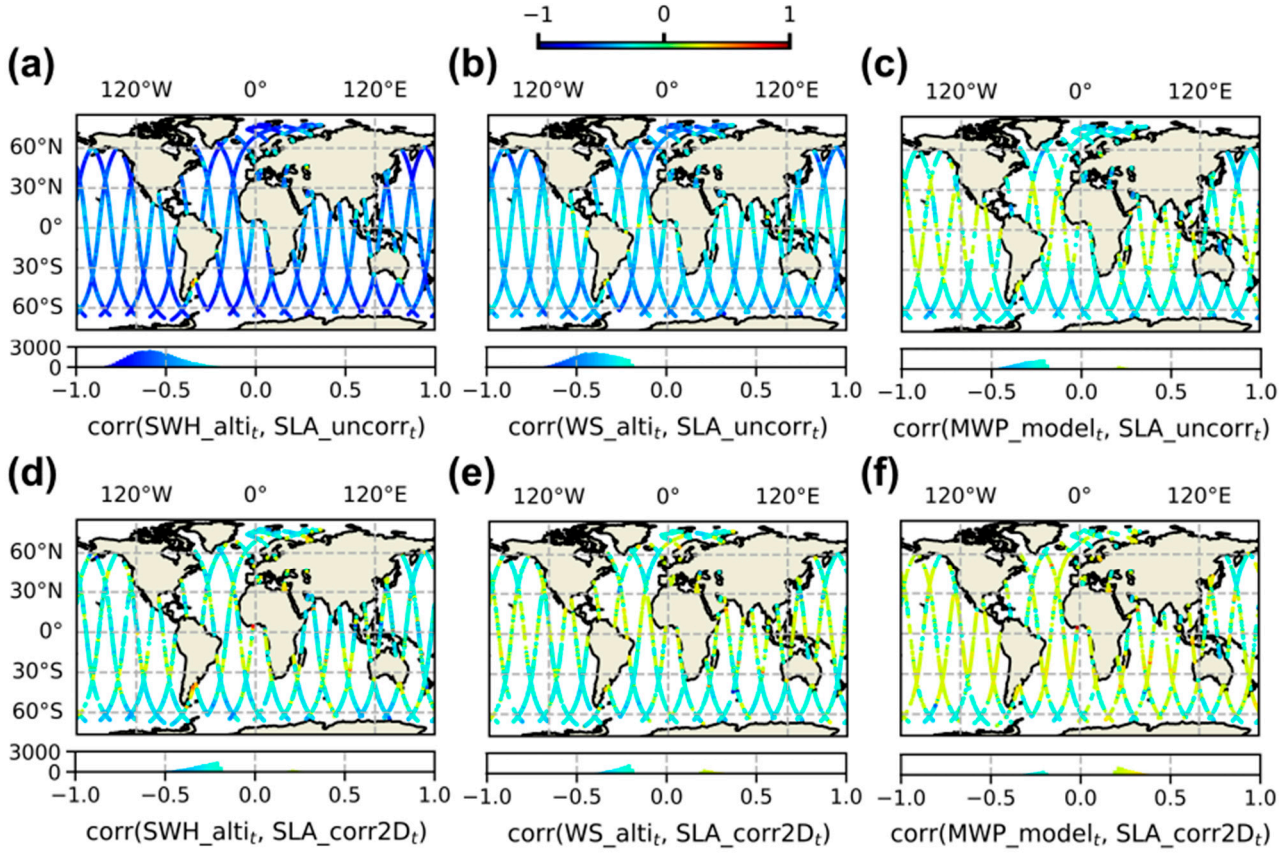

Figure 9. Maps of the cross-correlation values for the six (SSB input-related parameter, SLA) combinations mentioned in Table 3 at 0 day. The maps shown in (**a**–**c**) (resp., (**d**–**f**)) are associated with combinations involving SLA_uncorr (resp., SLA_corr2D). Non-significant correlations (i.e., falling within the 95% confidence interval) were removed from all maps, leaving an empty [−0.2, 0.2] range.

Overall, the results in the present section demonstrate that computing the cross-correlations between SLA and SSB descriptors can serve as an additional tool for evaluating (i) the relevance of potential SSB descriptor candidates and (ii) the performances of SSB corrections. Note that the relevance of a particular SSB descriptor candidate not only depends on its intrinsic capability to retain/describe SSB-related features but also on whether said candidate is correlated with the other prospective SSB descriptors and, hence, whether it provides redundant or new information.

4. Conclusions and Implications for SSB Modelling

SWOT 1-day fast-sampling phase data was exploited to evaluate assumptions currently used in SSB modelling. It was demonstrated that (i) ε can, indeed, as it is currently assumed, be considered as a zero-mean error term, and (ii) the DT associated with the three standard SSB descriptors (SWH, WS, and MWP) typically range from 1 to 4 days, with significant regional variations. The latter finding suggests that the formation of SSB databases through optimally time-differenced data points should be revisited whenever possible to ensure (as it is currently assumed) that the selected time-differenced data points originate from independent sea states. At the moment, the satellite-based observations feeding SSB models are typically separated by less than 10 days, but no lower limit on the selected time differencing intervals is applied. Provided that the orbit's repeat cycle of the mission at hand allows for it, future SSB models should rely on truly independent sea state observations, i.e., data points separated by, for instance, a minimum of 4 days. It could also be envisaged that SSB databases include time-differenced data points associated with regionally varying time

intervals; larger time intervals could be required in regions associated with more persistent features, and lower ones in regions exhibiting lower DTs.

The geographical distributions of the DT of SWH, WS, and MWP are also consistent with the general knowledge on global wind/wave circulation patterns. In short, high-latitude, rough wind/wave areas are associated with lower DT and, thus, less persistent features, because they are wind-coupled regions subject to strong and variable winds. In contrast, sea-state conditions in regions of weak/moderate wind fields are swell-dominated/low-SWH areas and depend more on swell variability. As a result, they exhibit longer-lasting features due to the oceanic system's inertia and higher DT dispersion ranges.

The SLA variance reductions found using differences in SLA adjusted using various SSB models, namely, 1D, 2D, and 3D corrections, are shown to increase steadily over the first five days and then reach a first plateau between ~5 and 15 days. Although a meticulous interpretation of the distinct behaviors observed before *versus* after 5 days is beyond the scope of the present study, such behaviors could tentatively be related to autocorrelations and/or cross-correlations among SSB descriptors. The present study showed that they are associated with decorrelation time scales on the order of a few days.

As expected, current SSB models rely on SSB descriptors that are often highly correlated with each other. The present study provides a precise quantification of these correlations and shows that the associated time scales are below or on the order of 1 day. Many of the observed correlations among SSB descriptors were attributed to atmospheric forcing with distinct behaviors occurring in swell and wind-sea-dominated areas. WS was found to be a short-term (up to +1 day) predictor of both SWH and MWP, while SWH appears to be a short-term (up to +1 day) predictor of MWP. Note that the predictive character of SWH over MWP does not necessarily imply that the two parameters are related through a direct causal relationship. Instead, it is likely that they present correlations because of their respective correlations with WS and other explanatory variables.

The correlations among SSB descriptors, although expected, were never precisely quantified before. Strong linear correlation between input model descriptors is commonly referred to as multicollinearity. Known issues related to multicollinearity can be generalized to predictive variables exhibiting nonlinear correlations (as it is the case for SSB descriptors), and include the development of models characterized by:

- Unnecessary complexity involving "excess" predictive variables;
- Bias and unreliability due to the redundancy of information comprised in the training dataset, which leads to overfitting;
- Instability when correlations among the predictive variables are period-dependent, since the developed models are then particularly sensitive to the considered dataset period.

Multicollinearity and impacts on SSB modelling can be investigated in future works to assess whether these issues affect SSB models. To overcome these potential issues, several methods could be envisaged, among which:

- Principal component analysis (PCA), which reduces the dimensionality associated with predictive variables by transforming the initial set of predictive variables into a new set of variables made of linear combinations of the original ones;
- Variable inflation factors, which evaluate the level of multicollinearity in a set of predictive variables, helping to select those that are the least correlated with each other;
- Regularization techniques, such as Lasso and Ridge regularizations, which rely on the addition of a penalty term to encourage the simplicity of the models, preventing overfitting;
- Classification approaches based on a partitioning of the sea-state conditions. Such approaches would allow for regionalizing the choices of SSB descriptors, thus producing class-specific SSB models, as tentatively conducted in [121,122].

The latest innovations in altimetry instruments and concepts, including delay-Doppler (SAR) altimetry and wide-swath interferometry (as SWOT KaRIn instrument), which both rely on synthetic Doppler aperture, have sparked a renewed interest in precise descriptions of the SSB, with the intention to further reduce its impact on mission error budgets. Synthetic Doppler aperture radars benefit from the satellite movement to create a synthetic antenna; they are, thus, affected by any surface movement, in addition to the other "classical" effects associated with conventional altimetry. As an example, SAR altimeter SSH and SWH estimates are affected by orbital wave velocities (induced by all sea-state conditions, not only swells) [123–130]. In addition, the finer along-track resolution provided by SAR altimetry (compared with conventional altimetry) introduces a high sensitivity to swell period and direction [131–133]. Methods specifically designed to correct altimetry measurements for these new effects are under active development [130,134–137]. Overall, the number of metocean variables required to extensively describe the processes at hand increases, resulting in the necessity to include a greater number of SSB descriptive variables. The push to consider and include new metocean variables to provide a finer description of the SSB makes the cross-correlations subject a particularly pressing one. We suggest that future works could focus on precisely assessing the impacts of multicollinearity on SSB modelling.

Finally, it was shown that computing the cross-correlations between SLA and SSB descriptors could serve as an additional tool for evaluating (i) the relevance of potential SSB descriptor candidates and (ii) the performances of SSB corrections. The former aspect can be assessed by computing the percentage of locations associated with significant (SSB descriptor candidate, SLA) correlations and the magnitude of said correlations, while the latter relies on the comparison of (SSB descriptor candidate, SLA) correlations before and after SLA is corrected for SSB (provided that the SSB model involves the SSB descriptor candidate). Note that the relevance of a particular SSB descriptor candidate also depends, as previously indicated, on whether said candidate provides redundant or new information, i.e., whether it is correlated with the other respective SSB descriptors. Finally, note that since the correlations between SLA and SSB descriptors are roughly limited to 0-day lags, it is reasonable to consider, as it is currently done, that SSB modelling does not require input from preceding days to provide an accurate description of the SSB.

We wish to stress that the unique nature of the SWOT 1-day repeat orbit dataset allowed for the exploration of new aspects related to the SSB. This dataset may be revisited or further exploited in the future to better inform the SSB or other related topics. Note that the 3.5-month observation period may not be long enough to confidently generalize all of the study's results. Consequently, future 1-day repeat orbits—if any—would surely be of paramount interest to the SSB community. In the present case, the study's DT results could not have been obtained based on 10-day (or more) repeat orbit datasets, as such orbits do not provide adequate temporal sampling to resolve average DT levels ranging from 1 to 4 days. For similar reasons, the time scales associated with cross-correlations (~few days) among SSB descriptors, on the one hand, and between SLA and SSB descriptors, on the other hand, could not have been resolved using 10-day (or more) repeat orbit datasets. Still, as the most widespread and most intense cross-correlations were shown to be "immediate" (i.e., occurring at 0-day lags), future works based on 10-day (or more) repeat orbit datasets could focus on computing the 0-day cross-correlations and would still provide useful information regarding both (i) the relevance of potential SSB descriptor candidates and (ii) the performances of SSB corrections.

Author Contributions: Conceptualization, N.T., L.A., D.V., and H.F.; methodology, E.M.; software, E.M.; validation, N.T., L.A., and E.M.; formal analysis, E.M.; investigation, E.M.; resources, F.B.-C. and G.D.; data curation, E.M.; writing—original draft preparation, E.M. and N.T.; writing—review and editing, E.M., N.T., L.A., D.V., H.F., G.D., and F.B.-C.; visualization, E.M.; supervision, N.T., L.A., F.B.-C., and G.D.; project administration, E.M. and F.B.-C.; funding acquisition, G.D. and F.B.-C. All authors have read and agreed to the published version of the manuscript.

Funding: French participation was funded by the French Space Agency (Centre National d'Etudes Spatiales) as part of the SALP project (221332). The contributions of D.V. and H.F. were performed and funded under ST13301CQ0050/1332KP22FNEED0042 via NOAA-NESDIS Ocean Surface Topography Science team support.

Data Availability Statement: The altimetry data were downloaded from Aviso+ via http://www.aviso.altimetry.fr, accessed on 1 October 2024. The Dynamic Atmospheric Correction (DAC) dataset dedicated to the SWOT fast-sampling phase (https://doi.org/10.24400/527896/A01-2023.019, accessed on 1 October 2024) was developed/validated by a LEGOS/CNRS/CLS team and distributed through Aviso+.

Acknowledgments: The authors would like to thank Hélène Roinard and her colleagues for building the SWOT nadir dataset, available at CLS, and the provision of the validity flag from cal/val activities to discard all questionable measurements. The authors would also like to thank the Reviewers for their helpful comments.

Conflicts of Interest: Authors Estelle Mazaleyrat, Ngan Tran and Laïba Amarouche were employed by the company Collecte Localisation Satellites, authors Douglas Vandemark and Hui Feng were employed by the company Global Science & Technology, Inc. The remaining authors declare that the research was conducted in the absence of any commercial or financial relationships that could be construed as a potential conflict of interest.

Appendix A

To support the choice of using L_2 estimates in the present study as estimates of the DT, a proper comparison of the L_0, L_{half}, L_1, and L_2 definitions (introduced in Section 2.4) was conducted. We remind the reader that L_0 (resp., L_{half}) assigned the DT to the time delay associated with the first ACF zero-crossing (resp., the first ACF 0.5 crossing), while L_1 and L_2 are defined as the discrete integrals of the ACF and squared ACF, respectively. More precisely, the L_1 integral is here (as it is usually done) computed between 0 and L_0, while L_2 is computed up to the largest (final) ACF time delay value.

First, the L_0, L_{half}, L_1, and L_2 definitions lead to analogous results whether the altimeter- or the model-based parameters are used (namely, SWH_alti *versus* SWH_model; and WS_alti *versus* WS_model). Figure A1 shows a comparison of the "matching" between the DT of the SWH computed with the altimeter-based (SWH_alti) and the model-based (SWH_model) time series for the L_0 (Figure A1a), L_{half} (Figure A1b), L_1 (Figure A1c), and L_2 (Figure A1d) definitions. The SWOT altimeter- and ERA5 model-based parameters were previously shown to provide very close values [138], hence—as expected—comparing DTs obtained with the altimeter- and model-based parameters provide high Pearson correlation coefficients; all four definitions are associated with coefficients above 0.86, indicated as "Corr(x,y)" at the top of each of the four plots. The best altimeter *versus* model match is found using the L_1 and L_2 definitions, both exhibiting a linear correlation coefficient equal to 0.94. Very similar results were obtained for WS_alti *versus* WS_model: the Pearson correlation coefficients amount to 0.83 for L_0; 0.92 for L_{half}; 0.91 for L_1; and 0.93 for L_2. As a result, so far, L_2 appears to be the best-suited definition for computing DT (the altimeter/model match obtained with L_2 is equal or superior to those found with the other three definitions).

Now turning to the global maps of the DTs, those associated with SWH_alti computed using the four considered DT definitions are presented in Figure A2. They show roughly similar geographical patterns (the color scales of the four maps were adjusted to find the best match). The greatest correspondence in terms of both geographical distributions and value ranges is found between the L_1 (Figure A2c) and L_2 (Figure A2d) maps, with values ranging (on average) from 1 to 4-5 days. Unsurprisingly, the L_0 (Figure A2a) and L_{half} (Figure A2b) maps are associated with, respectively, larger (~1–15 days) and smaller (~1–2 days) values, since the first ACF half-crossing (L_{half}) always precedes the first ACF zero-crossing (L_0).

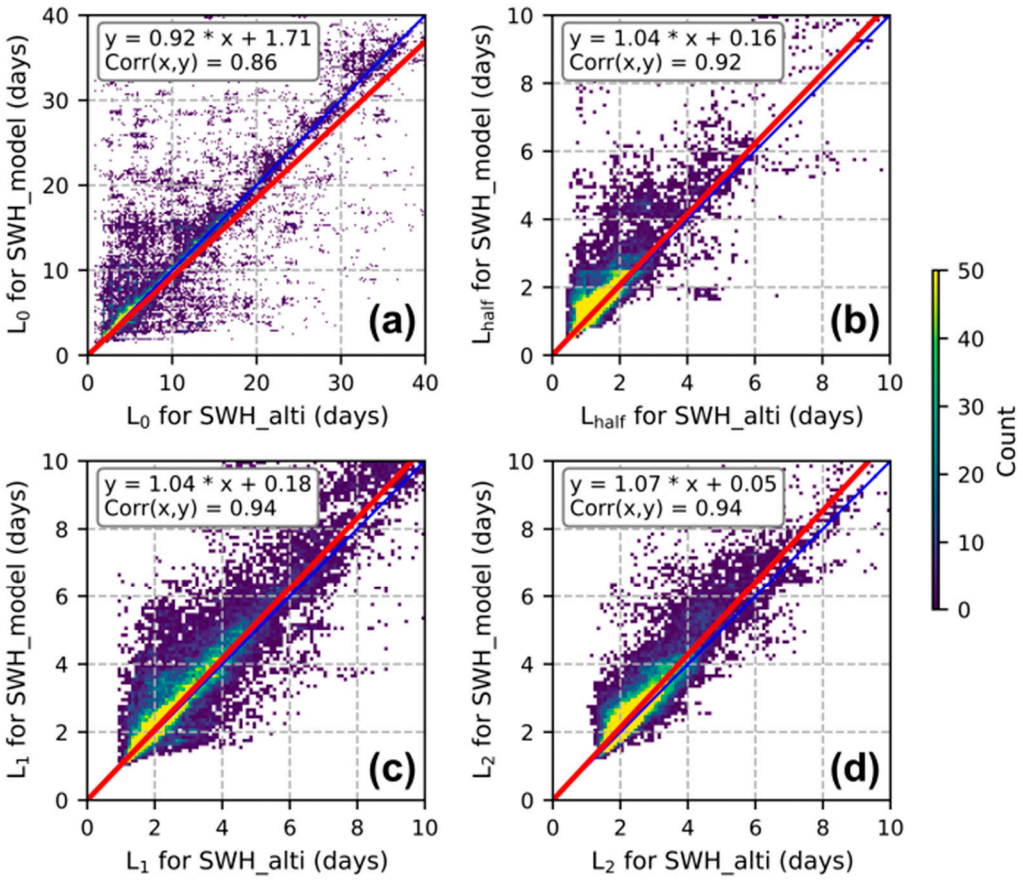

Figure A1. Comparison of the matching between the DTs of SWH_alti and SWH_model determined using the (**a**) L_0, (**b**) L_{half}, (**c**) L_1, and (**d**) L_2 definitions. For each plot, a linear regression is shown in red (with the associated fitted linear relationship and the Pearson correlation coefficient indicated in the top left corner) and the bisector in blue.

Regarding the distribution of the DTs on their respective ranges (illustrated in Figure A2 by histograms below each map), L_1 (Figure A2c) and L_2 (Figure A2d) are, again, the closest match, with a roughly bell-shaped distribution centered at around ~1.8 day. The observed undulations on the L_0 histogram (Figure A2a) are attributed to the non-monotonous behavior of the ACF around the zero-crossing axis, which results in the first zero-crossing L_0 discretized values. As for L_{half}, its histogram (bottom of Figure A2b) presents a step-like feature at around 1 day, which is absent from both the L_1 and L_2 histograms (Figure A2c,d). The absence of discretization and abrupt changes in the L_1 and L_2 histograms is attributed to the stability of the L_1 and L_2 definitions, which, contrary to L_0 and L_{half}, do not rely on a single point of the ACF, but rather an integral. These results suggest that the L_1 and L_2 definitions should be the preferred choices when computing DTs. Similar conclusions were drawn when analyzing the DTs of the other SSB input-related parameters considered in the present study.

Overall, L_2 appears to be the best-suited definition for computing the DT. The altimeter/model matching obtained with L_2 is equal or superior to those found with the other DT definitions, and the stability of the L_2 definition prevents any discretization or abrupt changes in its distribution. As a result, only L_2 DTs are presented in the main text of the present study.

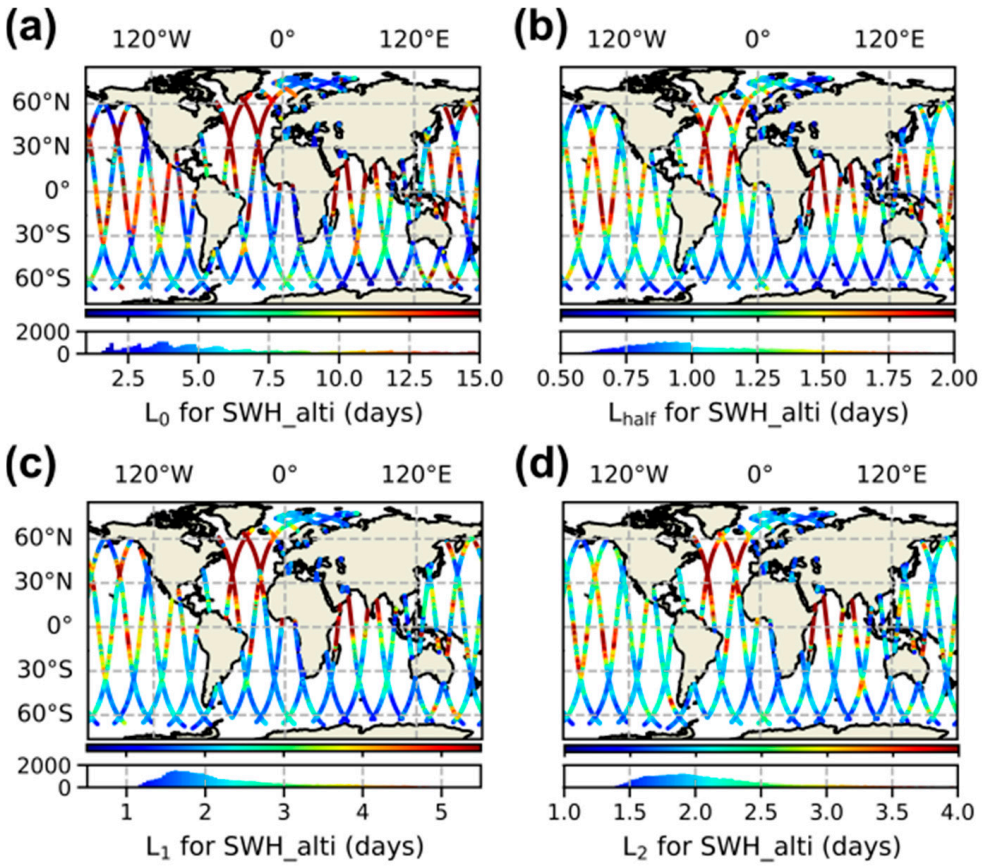

Figure A2. Maps of decorrelation time scales for SWH_alti computed using the (**a**) L_0; (**b**) L_{half}; (**c**) L_1; (**d**) L_2 definitions.

Appendix B

As mentioned in Section 3.2, one can display global maps of the ACFs at specific time delays rather than plot the ACFs as a function of the time delay at a few specific locations, the former type of figure offering a more global view of the ACF structure. Figure A3 provides such maps for WS_alti at +1 day (Figure A3a), +2 days (Figure A3b), and +3 days (Figure A3c). These maps are very consistent with those published by Monahan [80], derived from scatterometry SeaWinds data (see Figure 1, right panel, in [80]). The regions associated with high autocorrelation values (close to 1) after 3 days are associated with long DTs. As mentioned in the main text, the high DT values observed in the Arabian Sea are ascribed to the unique two-season weather pattern characteristics of the southwest monsoon, which leads to steady southwesterly wind speeds during our observation window [92–94]. Note that, similar to the present study, Monahan assumed stationarity for the surface vector winds. He also mentioned that the wind speed ACF maps are, for the most part, seasonally invariant, suggesting that it is reasonable, at least regarding WS, to generalize the results obtained in the present study (based on a 3.5-month window) for all seasons.

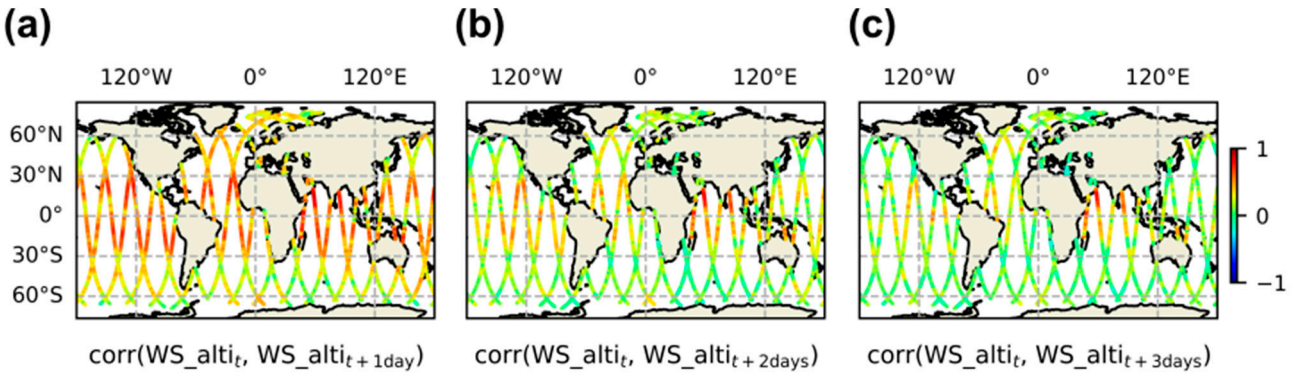

Figure A3. Autocorrelation maps of WS_alti: (**a**) +1 day; (**b**) +2 days; (**c**) +3 days.

References

1. Chelton, D.B.; Ries, J.C.; Haines, B.J.; Fu, L.L.; Callahan, P.S. Chapter 1: Satellite altimetry. In *Satellite Altimetry and Earth Sciences: A Handbook of Techniques and Applications*; Fu, L.-L., Cazenave, A., Eds.; International Geophysics; Academic Press: Cambridge, MA, USA, 2001; Volume 69, pp. i–ii. [CrossRef]
2. Escudier, P.; Couhert, A.; Mercier, F.; Mallet, A.; Thibaut, P.; Tran, N.; Amarouche, L.; Picard, B.; Carrere, L.; Dibarboure, G.; et al. Chapter Satellite Radar Altimetry Principle Accuracy and Precision. In *Satellite Altimetry over Oceans and Land Surfaces*; CRC Press: Boca Raton, FL, USA; Taylor & Francis Group: Abingdon, UK, 2017; pp. 1–70. [CrossRef]
3. Gourrion, J.; Vandemark, D.; Bailey, S.; Chapron, B.; Gommenginger, G.P.; Challenor, P.; Srokosz, M.A. A two-parameter wind speed algorithm for Ku-band altimeters. *J. Atmos. Ocean. Technol.* **2002**, *19*, 2030–2048. [CrossRef]
4. Collard, F. Algorithmes de vent et période moyenne des vagues JASON à base de réseaux de neurones (Algorithms for Jason wind speed and mean wave period based on neural network approach). BO-021-CLS-0407-RF. *Boost. Technol.* **2005**, *33*.
5. Abdalla, S. Ku-Band Radar Altimeter Surface Wind Speed Algorithm. *Mar. Geod.* **2012**, *35* (Suppl. S1), 276–298. [CrossRef]
6. Gaspar, P.; Ogor, F.; Le Traon, P.-Y.; Zanife, O.-Z. Estimating the sea state bias of the TOPEX and POSEIDON altimeters from crossover differences. *J. Geophys. Res. Ocean.* **1994**, *99*, 24981–24994. [CrossRef]
7. Gaspar, P.; Florens, J.-P. Estimation of the sea state bias in radar altimeter measurements of sea level: Results from a new nonparametric method. *J. Geophys. Res. Ocean.* **1998**, *103*, 15803–15814. [CrossRef]
8. Gaspar, P.; Labroue, S.; Ogor, F.; Lafitte, G.; Marchal, L.; Rafanel, M. Improving nonparametric estimates of the sea state bias in radar altimetry measurements of sea level. *J. Atmos. Ocean. Technol.* **2002**, *19*, 1690–1707. [CrossRef]
9. Tran, N.; Labroue, S.; Philipps, S.; Bronner, E.; Picot, N. Overview and update of the sea state bias corrections for the Jason-2, Jason-1 and TOPEX missions. *Mar. Geod.* **2010**, *33* (Suppl. S1), 348–362. [CrossRef]
10. Tran, N.; Thibaut, P.; Poisson, J.-C.; Philipps, S.; Bronner, E.; Picot, N. Impact of Jason-2 wind speed calibration on the sea state bias correction. *Mar. Geod.* **2011**, *34*, 407–419. [CrossRef]
11. Le Traon, P.-Y.; Nadal, F.; Ducet, N. An improved mapping method of multisatellite altimeter data. *J. Atmos. Ocean. Technol.* **1998**, *15*, 522–533. [CrossRef]
12. Pujol, M.-I.; Faugère, Y.; Taburet, G.; Dupuy, S.; Pelloquin, C.; Ablain, M.; Picot, N. DUACS DT2014: The new multimission altimeter data set reprocessed over 20 years. *Ocean Sci.* **2016**, *12*, 1067–1090. [CrossRef]
13. Taburet, G.; Sanchez-Roman, A.; Ballarotta, M.; Pujol, M.-I.; Legeais, J.-F.; Fournier, F.; Faugere, Y.; Dibarboure, G. DUACS DT2018: 25 years of reprocessed sea level altimetry products. *Ocean Sci.* **2019**, *15*, 1207–1224. [CrossRef]
14. Pujol, M.-I.; Dupuy, S.; Vergara, O.; Sánchez Román, A.; Faugère, Y.; Prandi, P.; Dabat, M.-L.; Dagneaux, Q.; Lievin, M.; Cadier, E.; et al. Refining the resolution of DUACS along-track level-3 sea level altimetry products. *Remote Sens.* **2023**, *15*, 793. [CrossRef]
15. Fu, L.-L.; Chelton, D.B.; Le Traon, P.-Y.; Morrow, R. Eddy dynamics from satellite altimetry. *Oceanography* **2010**, *23*, 14–25. [CrossRef]
16. Lee, T.; Hakkinen, S.; Kelly, K.; Qiu, B.; Bonekamp, H.; Lindstrom, E.J. Satellite observations of ocean circulation changes associated with climate variability. *Oceanography* **2010**, *23*, 70–81. [CrossRef]
17. Willis, J.K.; Chambers, D.P.; Kuo, C.-Y.; Shum, C.K. Global sea level rise: Recent progress and challenges for the decades to come. *Oceanography* **2010**, *23*, 26–35. [CrossRef]
18. Ballarotta, M.; Ubelmann, C.; Pujol, M.-I.; Taburet, G.; Legeais, J.-F.; Faugere, Y.; Delepoulle, A.; Chelton, D.; Dibarboure, G.; Picot, N. On the resolution of ocean altimetry maps. *Ocean Sci.* **2019**, *15*, 1091–1109. [CrossRef]
19. Chelton, D.B.; Schlax, M.G. The accuracies of smoothed sea surface height fields constructed from tandem satellite altimeter datasets. *J. Atmos. Ocean. Technol.* **2003**, *20*, 1276–1302. [CrossRef]
20. Wunsch, C. Toward a midlatitude ocean frequency–wavenumber spectral density and trend determination. *J. Phys. Oceanogr.* **2010**, *40*, 2264–2281. [CrossRef]
21. Dibarboure, G.; Morrow, R. Value of the Jason-1 geodetic phase to study rapid oceanic changes and importance for defining a Jason-2 geodetic orbit. *J. Atmos. Ocean. Technol.* **2016**, *33*, 1913–1930. [CrossRef]

22. Fu, L.-L.; Ubelmann, C. On the transition from profile altimeter to swath altimeter for observing global ocean surface topography. *J. Atmos. Ocean. Technol.* **2014**, *31*, 560–568. [CrossRef]
23. Morrow, R.; Fu, L.-L.; Ardhuin, F.; Benkiran, M.; Chapron, B.; Cosme, E.; d'Ovidio, F.; Farrar, J.T.; Gille, S.T.; Lapeyre, G.; et al. Global observations of fine-scale ocean surface topography with the Surface Water and Ocean Topography (SWOT) mission. *Front. Mar. Sci.* **2019**, *6*, 232. [CrossRef]
24. d'Ovidio, F.; Pascual, A.; Wang, J.; Doglioli, A.M.; Jing, Z.; Moreau, S.; Grégori, G.; Swart, S.; Speich, S.; Cyr, F.; et al. Frontiers in fine-scale in situ studies: Opportunities during the SWOT fast sampling phase. *Front. Mar. Sci.* **2019**, *6*, 168. [CrossRef]
25. Fu, L.-L.; Pavelsky, T.; Cretaux, J.-F.; Morrow, R.; Farrar, J.T.; Vaze, P.; Sengenes, P.; Vinogradova-Shiffer, N.; Sylvestre-Baron, A.; Picot, N.; et al. The surface water and ocean topography mission: A breakthrough in radar remote sensing of the ocean and land surface water. *Geophys. Res. Lett.* **2024**, *51*, e2023GL107652. [CrossRef]
26. QUID Document for WAVE TAC Product WAVE_GLO_PHY_SWH_L3_NRT_014_001. Available online: https://catalogue.marine.copernicus.eu/documents/QUID/CMEMS-WAV-QUID-014-001.pdf (accessed on 1 October 2024).
27. QUID Document for WAVE TAC Product WAVE_GLO_PHY_SWH_L4_NRT_014_003. Available online: https://catalogue.marine.copernicus.eu/documents/QUID/CMEMS-WAV-QUID-014-003.pdf (accessed on 1 October 2024).
28. Woo, H.-J.; Park, K.-A. Validation of significant wave height from Jason-3 and Sentinel-3A/B and relation to tidal currents in coastal regions of the Korean Peninsula. *Int. J. Remote Sens.* **2022**, *43*, 961–996. [CrossRef]
29. Jiang, M.; Xu, K.; Wang, J. Evaluation of Sentinel-6 altimetry data over ocean. *Remote Sens.* **2023**, *15*, 12. [CrossRef]
30. Yang, J.; Zhang, J.; Jia, Y.; Fan, C.; Cui, W. Validation of Sentinel-3A/3B and Jason-3 altimeter wind speeds and significant wave heights using buoy and ASCAT data. *Remote Sens.* **2020**, *12*, 2079. [CrossRef]
31. Abdalla, S.; Janssen, P.A.E.M.; Bidlot, J.-R. Altimeter near real time wind and wave products: Random error estimation. *Mar. Geod.* **2011**, *34*, 393–406. [CrossRef]
32. Tran, N.; Vandemark, D.; Labroue, S.; Feng, H.; Chapron, B.; Tolman, H.L.; Lambin, J.; Picot, N. Sea state bias in altimeter sea level estimates determined by combining wave model and satellite data. *J. Geophys. Res. Ocean.* **2010**, *115*, C03020. [CrossRef]
33. Tran, N.; Vandemark, D.; Zaron, E.D.; Thibaut, P.; Dibarboure, G.; Picot, N. Assessing the effects of sea-state related errors on the precision of high-rate Jason-3 altimeter sea level data. *Adv. Space Res.* **2021**, *68*, 963–977. [CrossRef]
34. Raynal, M.; Bohe, A.; Picot, N.; Dibarboure, G.; Prandi, P.; Nencioli, F.; Cadier, E.; Delepoulle, A.; Ubelmann, C.; Picard, B.; et al. KaRIn performances and validation over open ocean. In Proceedings of the SWOT Science Team Meeting 2024, Chapel Hill, NC, USA, 17–21 June 2024. Available online: https://swotst.aviso.altimetry.fr/fileadmin/user_upload/SWOTST2024/20240618/10_Tue_AM_Raynal_KaRIn_LR_Validation.pdf (accessed on 1 October 2024).
35. Morrow, R.; Blumstein, D.; Dibarboure, G. Chapter 8: Fine-scale altimetry and the future SWOT mission. In *New Frontiers in Operational Oceanography*; Chassignet, E.P., Pascual, A., Tintoré, J., Verron, J., Eds.; GODAE OceanView: Tallahassee, FL, USA, 2018; pp. 191–226. [CrossRef]
36. SWOT Nadir Altimetry Interim Geophysical Data Records (Swot NATL IGDR). Available online: https://www.aviso.altimetry.fr/en/data/products/sea-surface-height-products/global/gdr-igdr-and-ogdr.html (accessed on 1 October 2024).
37. Amarouche, L.; Thibaut, P.; Zanife, O.-Z.; Dumont, J.P.; Vincent, P.; Steunou, N. Improving the Jason-1 ground retracking to better account for attitude effects. *Mar. Geod.* **2004**, *27*, 171–197. [CrossRef]
38. Thibaut, P.; Poisson, J.-C.; Bronner, E.; Picot, N. Relative performance of the MLE3 and MLE4 retracking algorithms on Jason-2 altimeter waveforms. *Mar. Geod.* **2010**, *33* (Suppl. S1), 317–335. [CrossRef]
39. Lyard, F.; Carrere, L.; Dabat, M.; Tchilibou, M.; Fouchet, E.; Faugère, Y.; Dibarboure, G.; Picot, N. Barotropic corrections for SWOT: FES2022 and DAC. In Proceedings of the SWOT Meeting, Toulouse, France, 21 September 2023.
40. Dynamic Atmospheric Correction dedicated to SWOT CalVal Phase. Available online: https://www.aviso.altimetry.fr/en/data/products/auxiliary-products/dynamic-atmospheric-correction-dedicated-to-swot-calval-phase/description.html (accessed on 1 October 2024).
41. Hersbach, H.; Bell, B.; Berrisford, P.; Hirahara, S.; Horányi, A.; Muñoz-Sabater, J.; Nicolas, J.; Peubey, C.; Radu, R.; Schepers, D.; et al. The ERA5 global reanalysis. *Quaterly J. R. Meteorol. Soc.* **2020**, *146*, 1999–2049. [CrossRef]
42. Yaplee, B.S.; Shapiro, A.; Hammond, D.L.; Au, B.D.; Uliana, E.A. Nanosecond radar observations of the ocean surface from a stable platform. *IEEE Trans. Geosci. Electron.* **1971**, *9*, 170–174. [CrossRef]
43. Vandemark, D.; Tran, N.; Beckley, B.D.; Chapron, B.; Gaspar, P. Direct estimation of sea state impacts on radar altimeter sea level measurements. *Geophys. Res. Lett.* **2002**, *29*, 2148. [CrossRef]
44. Feng, H.; Yao, S.; Li, L.; Tran, N.; Vandemark, D.; Labroue, S. Spline-based nonparametric estimation of the altimeter sea-state bias correction. *IEEE Geosci. Remote Sens. Lett.* **2010**, *7*, 577–581. [CrossRef]
45. Chambers, D.P.; Hayes, S.A.; Ries, J.C.; Urban, T.J. New TOPEX sea state bias models and their effect on global mean sea level. *J. Geophys. Res. Ocean.* **2003**, *108*, 3305. [CrossRef]
46. Labroue, S.; Gaspar, P.; Dorandeu, J.; Zanife, O.-Z.; Mertz, F.; Vincent, P.; Choquet, D. Nonparametric estimates of the sea state bias for Jason-1 radar altimeter. *Mar. Geod.* **2004**, *27*, 453–481. [CrossRef]
47. Gommenginger, C.; Srokosz, M.; Bellingham, C.; Snaith, H.; Pires, N.; Fernandes, M.J.; Tran, N.; Vandemark, D.; Moreau, T.; Labroue, S.; et al. Sea state bias: 25 years on. In Proceedings of the 25 Years of Progress in Radar Altimetry 2018, Ponta Delgada, Portugal, 24–29 September 2018.

48. Pires, N.; Fernandes, M.J.; Gommenginger, C.; Scharroo, R. A conceptually simple modeling approach for Jason-1 sea state bias correction based on 3 parameters exclusively derived from altimetric information. *Remote Sens.* **2016**, *8*, 576. [CrossRef]
49. Pires, N.; Fernandes, M.J.; Gommenginger, C.; Scharroo, R. Improved sea state bias estimation for altimeter reference missions with altimeter-only three-parameter models. *IEEE Trans. Geosci. Remote Sens.* **2019**, *57*, 1448–1462. [CrossRef]
50. Jiang, M.; Xu, K.; Liu, Y.; Wang, L. Estimating the sea state bias of Jason-2 altimeter from crossover differences by using a three-dimensional nonparametric model. *IEEE J. Sel. Top. Appl. Earth Obs. Remote Sens.* **2016**, *9*, 5023–5043. [CrossRef]
51. Jiang, H.; Stopa, J.E.; Wang, H.; Husson, R.; Mouche, A.; Chapron, B.; Chen, G. Tracking the attenuation and nonbreaking dissipation of swells using altimeters. *J. Geophys. Res. Ocean.* **2016**, *121*, 1446–1458. [CrossRef]
52. Millet, F.W.; Warnick, K.F.; Nagel, J.R.; Arnold, D.V. Physical optics-based electromagnetic bias theory with surface height-slope cross-correlation and hydrodynamic modulation. *IEEE Trans. Geosci. Remote Sens.* **2006**, *44*, 1470–1483. [CrossRef]
53. Tran, N.; Amarouche, L.; Kocha, C.; Rialland, R.; Quet, V.; Grau, C.; Ollivier, A.; Daguze, J.-A.; Pirotte, T.; Maraldi, C.; et al. SSB modeling from CFOSAT data. In Proceedings of the Ocean Surface Topography Science Team Meeting, Puerto Rico, WV, USA, 7–11 November 2023. Available online: https://ostst.aviso.altimetry.fr/fileadmin/user_upload/OSTST2023/Presentations/CFO2023-SSB_modeling_from_CFOSAT_data.pdf (accessed on 1 October 2024).
54. Bignalet-Cazalet, F.; Picot, N.; Desai, S.; Scharroo, R.; Egido, A. Jason-3 Products Handbook. 2021. Available online: https://www.aviso.altimetry.fr/fileadmin/documents/data/tools/hdbk_j3.pdf (accessed on 1 October 2024).
55. Labroue, S.; Gaspar, P.; Dorandeu, J.; Mertz, F.; Tran, N.; Zanife, O.-Z.; Vincent, P.; Picot, N.; Femenias, P. Overview of the Improvements Made on the Empirical Determination of the Sea State Bias Correction. In Proceedings of the 15 Years of Progress in Radar Altimetry Symposium, Venice, Italy, 13–18 March 2006. Available online: https://citeseerx.ist.psu.edu/document?repid=rep1&type=pdf&doi=e7a8d3542c2faadaafbe0988990202fb230f4a89 (accessed on 1 October 2024).
56. Paige, C.C.; Saunders, A.M. LSQR: An algorithm for sparse linear equations and sparse least squares. *ACM Trans. Math. Softw.* **1982**, *8*, 43–71. [CrossRef]
57. Fong, D.C.-L.; Saunders, M. LSMR: An iterative algorithm for sparse least-squares problems. *SIAM J. Sci. Comput.* **2011**, *33*, 2950–2971. [CrossRef]
58. Ozger, M. Scaling characteristics of ocean wave height time series. *Phys. A Stat. Mech. Its Appl.* **2011**, *390*, 981–989. [CrossRef]
59. Olivares, F.; Zunino, L. Multiscale dynamics under the lens of permutation entropy. *Phys. A Stat. Mech. Its Appl.* **2020**, *559*, 125081. [CrossRef]
60. Kavasseri, R.G.; Nagarajan, R. Evidence of crossover phenomena in wind-speed data. *IEEE Trans. Circuits Syst. I Regul. Pap.* **2004**, *51*, 2255–2562. [CrossRef]
61. Olivares, F.; Zunino, L.; Rosso, O.A. Quantifying long-range correlations with a multiscale ordinal pattern approach. *Phys. A Stat. Mech. Its Appl.* **2016**, *445*, 283–294. [CrossRef]
62. Russo, D.; Jury, W.A. A theoretical study of the estimation of the correlation scale in spatially variable fields: 1. Stationary fields. *Water Resour. Res.* **1987**, *23*, 1257–1268. [CrossRef]
63. Blöschl, G. Scaling issues in snow hydrology. *Hydrol. Process.* **1999**, *13*, 2149–2175. [CrossRef]
64. Skøien, J.O.; Blöschl, G. Sampling scale effects in random fields and implications for environmental monitoring. *Environ. Monit. Assess.* **2006**, *114*, 521–552. [CrossRef] [PubMed]
65. Smith, B.L.; Neal, D.R.; Feero, M.; Richards, G. Assessing the limitations of effective number of samples for finding the uncertainty of the mean correlated data. *Meas. Sci. Technol.* **2018**, *29*, 125304. [CrossRef]
66. Snaith, H.M.; Robinson, I.S. A study of currents south of Africa using Geosat satellite altimetry. *J. Geophys. Res. Ocean.* **1996**, *101*, 18141–18154. [CrossRef]
67. Richman, J.G.; Wunsch, C.; Hogg, N.G. Space and time scales of mesoscale motion in the Western North Atlantic. *Rev. Geophys.* **1977**, *15*, 385–420. [CrossRef]
68. Le Traon, P.-Y.; Rouquet, M.C.; Boissier, C. Spatial scales of mesoscale variability in the North Atlantic as deduced from Geosat data. *J. Geophys. Res. Ocean.* **1990**, *95*, 20267–20285. [CrossRef]
69. Le Traon, P.-Y. Time scales of mesoscale variability and their relationship with space scales in the North Atlantic. *J. Mar. Res.* **1991**, *49*, 467–492. [CrossRef]
70. Stammer, D. Global characteristics of ocean variability estimated from regional TOPEX/POSEIDON altimeter measurements. *J. Phys. Oceanogr.* **1997**, *27*, 1743–1769. [CrossRef]
71. Katz, R.W. Use of cross correlations in the search for teleconnections. *J. Climatol.* **1988**, *8*, 241–253. [CrossRef]
72. Akaike, H. A new look at the statistical model identification. *IEEE Trans. Autom. Control* **1974**, *19*, 716–723. [CrossRef]
73. Tran, N.; Vandemark, D.; Chapron, B.; Labroue, S.; Feng, H.; Beckley, B.; Vincent, P. New models for satellite altimeter sea state bias correction developed using wave model data. *J. Geophys. Res. Ocean.* **2006**, *111*, C09009. [CrossRef]
74. Dickey, D.A.; Fuller, W.A. Distribution of the estimators of autoregressive time series with a unit root. *J. Am. Stat. Assoc.* **1979**, *74*, 427–431. [CrossRef]
75. Dickey, D.A.; Fuller, W.A. Likelihood ratio statistics for autoregressive time series with unit root. *Econometrica* **1981**, *49*, 1057–1072. [CrossRef]
76. Kavasseri, R.G.; Seetharaman, K. Day-ahead wind speed forecasting using f-ARIMA models. *Renew. Energy* **2009**, *34*, 1388–1393. [CrossRef]

77. Yuan, X.; Tan, Q.; Lei, X.; Yuan, Y.; Wu, X. Wind power prediction using hybrid autoregressive fractionally integrated moving average and least square support vector machine. *Energy* **2017**, *129*, 122–137. [CrossRef]
78. Geweke, J.; Porter-Hudak, S. The estimation and application of long memory time series models. *J. Time Ser. Anal.* **1983**, *4*, 221–238. [CrossRef]
79. Reisen, V.A. Estimation of the fractional difference parameter in the ARFIMA(p,d,q) model using the smoothed periodogram. *J. Time Ser. Anal.* **1994**, *15*, 335–350. [CrossRef]
80. Monahan, A.H. The temporal autocorrelation structure of sea surface winds. *J. Clim.* **2012**, *25*, 6684–6700. [CrossRef]
81. Trenberth, K.E.; Jones, P.D.; Ambenje, P.; Bojariu, R.; Easterling, D.; Klein Tank, A.; Parker, D.; Rahimzadeh, F.; Renwick, J.A.; Rusticucci, M.; et al. Observations: Surface and Atmospheric Climate Change. In *Climate Change 2007: The Physical Science Basis*; Contribution of Working Group I to the Fourth Assessment Report of the Intergovernmental Panel on Climate Change; Solomon, S., Qin, D., Manning, M., Chen, Z., Marquis, M., Averyt, K.B., Tignor, M., Miller, H.L., Eds.; Cambridge University Press: Cambridge, UK; New York, NY, USA, 2007.
82. Trigo, R.M.; Valente, M.A.; Trigo, I.F.; Miranda, P.M.A.; Ramos, A.M.; Paredes, D.; García-Herrera, R. The impact of North Atlantic wind and cyclone trends on European precipitation and significant wave height in the Atlantic. *Ann. N. Y. Acad. Sci.* **2008**, *1146*, 212–234. [CrossRef]
83. Semedo, A.; Sušelj, K.; Rutgersson, A.; Sterl, A. A global view on the wind sea and swell climate and variability from ERA-40. *J. Clim.* **2011**, *24*, 1461–1479. [CrossRef]
84. Ardhuin, F.; Chapron, B.; Collard, F. Observation of swell dissipation across oceans. *Geophys. Res. Lett.* **2009**, *36*, L06607. [CrossRef]
85. Zheng, C.W.; Li, C.Y.; Pan, J. Propagation route and speed of swell in the Indian Ocean. *J. Geophys. Res. Ocean.* **2018**, *123*, 8–21. [CrossRef]
86. Chen, G.; Chapron, B.; Ezraty, R.; Vandemark, D. A global view of swell and wind sea climate in the ocean by satellite altimeter and scatterometer. *J. Atmos. Ocean. Technol.* **2002**, *19*, 1849–1859. [CrossRef]
87. Chen, G.; Ezraty, R.; Fang, C.; Fang, L. A new look at the zonal pattern of the marine wind system from TOPEX measurements. *Remote Sens. Environ.* **2002**, *79*, 15–22. [CrossRef]
88. Alves, J.H.G.M. Numerical modeling of ocean swell contributions to the global wind-wave climate. *Ocean Model.* **2006**, *11*, 98–122. [CrossRef]
89. Li, X.-M. A new insight from space into swell propagation and crossing in the global oceans. *Geophys. Res. Lett.* **2016**, *43*, 5202–5209. [CrossRef]
90. Ardhuin, F.; Stopa, J.E.; Chapron, B.; Collard, F.; Husson, R.; Jensen, R.E.; Johannessen, J.; Mouche, A.; Passaro, M.; Quartly, G.D.; et al. Observing sea states. *Front. Mar. Sci.* **2019**, *6*, 124. [CrossRef]
91. Jiang, H.; Mu, L. Wave climate from spectra and its connections with local and remote wind climate. *J. Phys. Oceanogr.* **2019**, *49*, 543–559. [CrossRef]
92. Halpern, D.; Freilich, M.H.; Weller, R.A. Arabian sea surface winds and ocean transports determined from ERS-1 scatterometer. *J. Geophys. Res. Ocean.* **1998**, *103*, 7799–7805. [CrossRef]
93. Goswami, B.N.; Sengupta, D.; Kumar, G.S. Intraseasonal oscillations and interannual variability of surface winds over the Indian monsoon region. *Proc. Indian Acad. Sci. Earth Planet. Sci.* **1998**, *107*, 45–64. [CrossRef]
94. Dai, L.; Cheng, T.F.; Wang, B.; Lu, M. Subseasonal features of the Indian monsoon. *J. Clim.* **2023**, *36*, 7199–7211. [CrossRef]
95. Ebuchi, N.; Kawamura, H.; Toba, Y. Growth of wind waves with fetch observed by the Geosat altimeter in the Japan Sea under winter monsoon. *J. Geophys. Res. Ocean.* **1992**, *97*, 809–819. [CrossRef]
96. Young, I.R. Seasonal variability of the global ocean wind and wave climate. *Int. J. Climatol.* **1999**, *19*, 931–950. [CrossRef]
97. Zhang, X.; Wu, K.; Li, R.; Li, D.; Zhang, S.; Zhang, R.; Li, S.; Dong, X. Analysis of the interannual variability of Pacific swell pools. *J. Mar. Sci. Eng.* **2023**, *11*, 1883. [CrossRef]
98. Johnson, G.; Kumar, V.; Chempalayil, S.; Singh, J.; Pednekar, P.; Kumar, K.; Dora, G.; Gowthaman, R. Variations in swells along Eastern Arabian Sea during the summer monsoon. *Open J. Mar. Sci.* **2012**, *2*, 43–50. [CrossRef]
99. Zheng, K.; Sun, J.; Guan, C.; Shao, W. Analysis of the global swell and wind sea energy distribution using WAVEWATCH III. *Adv. Meteorol.* **2016**, *2016*, 8419580. [CrossRef]
100. Gulev, S.K.; Grigorieva, V. Variability of the winter wind waves and swell in the North Atlantic and North Pacific as revealed by the voluntary observing ship data. *J. Clim.* **2006**, *19*, 5667–5685. [CrossRef]
101. Semedo, A. Seasonal variability of wind sea and swell waves climate along the Canary current: The local wind effect. *J. Mar. Sci. Eng.* **2018**, *6*, 28. [CrossRef]
102. Colosi, L.V.; Villas Bôas, A.B.; Gille, S.T. The seasonal cycle of significant wave height in the ocean: Local versus remote forcing. *J. Geophys. Res. Ocean.* **2021**, *126*, e2021JC017198. [CrossRef]
103. Feng, X.; Tsimplis, M.N.; Quartly, G.D.; Yelland, M.J. Wave height analysis from 10 years of observations in the Norwegian Sea. *Cont. Shelf Res.* **2014**, *72*, 47–56. [CrossRef]
104. Johnstone, J.; Curry, J. What's Causing the Extremely Warm Temperatures in the North Atlantic? Web *Blog Post*. 2023. Available online: https://judithcurry.com/2023/07/02/whats-causing-the-extremely-warm-temperatures-in-the-north-atlantic/ (accessed on 1 October 2024).

105. Li, X.; Tan, W.; Hu, Z.-Z.; Johnson, N.C. Evolution and prediction of two extremely strong Atlantic Niños in 2019–2021: Impact of Benguela warming. *Geophys. Res. Lett.* **2023**, *50*, e2023GL104215. [CrossRef]
106. Zhang, L.; Wang, C.; Han, W.; McPhaden, M.J.; Hu, A.; Xing, W. Emergence of the Central Atlantic Niño. *Sci. Adv.* **2023**, *9*, eadi5507. [CrossRef] [PubMed]
107. Ljung, G.M.; Box, G.E.P. On a measure of lack of fit in time series models. *Biometrika* **1978**, *65*, 297–303. [CrossRef]
108. Haselsteiner, A.F.; Coe, R.G.; Manuel, L.; Chai, W.; Leira, B.; Clarindo, G.; Guedes Soares, C.; Hannesdóttir, Á.; Dimitrov, N.; Sander, A.; et al. A benchmarking exercise for environmental contours. *Ocean Eng.* **2021**, *236*, 109504. [CrossRef]
109. Carter, D. Prediction of wave height and period for a constant wind velocity using the JONSWAP results. *Ocean Eng.* **1982**, *9*, 17–33. [CrossRef]
110. Hwang, P.A.; Teague, W.J.; Jacobs, G.A.; Wang, D.W. A statistical comparison of wind speed, wave height, and wave period derived from satellite altimeters and ocean buoys in the Gulf of Mexico region. *J. Geophys. Res. Ocean.* **1998**, *103*, 10451–10468. [CrossRef]
111. Bidlot, J.R. Ocean Wave Model Output Parameters. Technical Report ECMWF. 2016. Available online: https://confluence.ecmwf.int/download/attachments/59774192/wave_parameters.pdf?version=1 (accessed on 1 October 2024).
112. Stopa, J.E.; Ardhuin, F.; Babanin, A.; Zieger, S. Comparison and validation of physical wave parameterizations in spectral wave models. *Ocean Model.* **2016**, *103*, 2–17. [CrossRef]
113. Chun, H.; Suh, K.D. Estimation of significant wave period from wave spectrum. *Ocean Eng.* **2018**, *163*, 609–616. [CrossRef]
114. Hasselmann, K.; Barnett, T.P.; Bouws, E.; Carlson, H.; Cartwright, D.E.; Enke, K.; Ewing, J.A.; Gienapp, H.; Hasselmann, D.E.; Kruseman, P.; et al. Measurements of wind-wave growth and swell decay during the Joint North Sea Wave Project (JONSWAP). *Ergänzungsheft Zur Dtsch. Hydrogr. Z. Reihe A* **1973**, *12*, 1–95.
115. Hasselmann, K.; Sell, W.; Ross, D.B.; Müller, P. A parametric wave prediction model. *J. Phys. Oceanogr.* **1976**, *6*, 200–228. [CrossRef]
116. Toba, Y. Stochastic form of the growth of wind waves in a single-parameter representation with physical implications. *J. Phys. Oceanogr.* **1978**, *8*, 494–507. [CrossRef]
117. Stopa, J.E.; Cheung, K.F.; Tolman, H.L.; Chawla, A. Patterns and cycles in the Climate Forecast System Reanalysis wind and wave data. *Ocean Model.* **2013**, *70*, 207–220. [CrossRef]
118. Niu, Y.; Guo, B.; Subrahmanyam, M.V.; Xue, B.; Ye, Y. The influence of typhoon "MITAG" on waves and currents in Zhoushan Sea area, China. *Atmosphere* **2021**, *12*, 1027. [CrossRef]
119. Parvaresh, A.; Hassanzadeh, S.; Bordbar, M.H. Statistical analysis of wave parameters in the north coast of the Persian Gulf. *Ann. Geophys.* **2005**, *23*, 2031–2038. [CrossRef]
120. Stefanakos, C.N.; Belibassakis, K.A. Nonstationary stochastic modelling of multivariate long-term wind and wave data. In Proceedings of the International Conference on Offshore Mechanics and Arctic Engineering, Halkidiki, Greece, 12–17 June 2005; pp. 225–234. [CrossRef]
121. Feng, H.; Vandemark, D.; Chapron, B.; Tran, N.; Beckley, B. Use of fuzzy logic clustering analysis to address wave impacts on altimeter sea level measurements: Part I data classification. In Proceedings of the Ocean Surface Topography Science Team Meeting 2006, Venice, Italy, 16–18 March 2006. Available online: https://www.aviso.altimetry.fr/fileadmin/documents/OSTST/2006/feng.pdf (accessed on 1 October 2024).
122. Vandemark, D.; Feng, H.; Chapron, B.; Tran, N.; Beckley, B. Use of fuzzy logic clustering analysis to address wave impacts on altimeter sea level measurements: Part II results. In Proceedings of the Ocean Surface Topography Science Team Meeting 2006, Venice, Italy, 16–18 March 2006. Available online: https://www.aviso.altimetry.fr/fileadmin/documents/OSTST/2006/vandemark.pdf (accessed on 1 October 2024).
123. Boisot, O.; Amarouche, L.; Lalaurie, J.-C.; Guérin, C.-A. Dynamical properties of sea surface microwave backscatter at low-incidence: Correlation time and Doppler shift. *IEEE Trans. Geosci. Remote Sens.* **2016**, *54*, 7385–7395. [CrossRef]
124. Amarouche, L.; Tran, N.; Herrera, D.; Guerin, C.; Dubois, P.; Aublanc, J.; Boy, F. Impact of the ocean waves motion on the Delay/Doppler altimeters measurements. In Proceedings of the Ocean Surface Topography Science Team Meeting 2019, Chicago, IL, USA, 21–25 October 2019. Available online: https://ostst.aviso.altimetry.fr/fileadmin/user_upload/OSTST2019/IPM_05_Amarouche_DopplerWavesSARMode_OSTST2019_Final.pdf (accessed on 1 October 2024).
125. Buchhaupt, C. Model Improvement for SAR Altimetry. Ph.D. Thesis, Schriftenreihe Fachrichtung Geodäsie der Technischen Universität Darmstadt, Darmstadt, Germany, 2019. ISBN 978-3-935631-44-0. Available online: https://tuprints.ulb.tu-darmstadt.de/9015/ (accessed on 1 October 2024).
126. Egido, A.; Ray, C. On the effect of surface motion in SAR altimeter observations of the open ocean. In Proceedings of the Ocean Surface Topography Science Team Meeting 2019, Chicago, IL, USA, 21–25 October 2019. Available online: https://ostst.aviso.altimetry.fr/fileadmin/user_upload/OSTST2019/IPM_03_Egido20191022_-_OSTST_-_AEE.pdf (accessed on 1 October 2024).
127. Raynal, M.; Cadier, E.; Labroue, S.; Moreau, T.; Rieu, P.; Féménias, P.; Bordes, F.; Boy, F.; Picot, N. Lessons Learned from Sentinel SARM Missions in Preparation of Jason-CS. In Proceedings of the Ocean Surface Topography Science Team Meeting, Chicago, IL, USA, 21–25 October 2019. Available online: https://ostst.aviso.altimetry.fr/fileadmin/user_upload/OSTST2019/ERR_04_SARM_lessons_learned_raynal.pdf (accessed on 1 October 2024).

128. Tran, N.; Amarouche, L.; Boy, F. Impact of the ocean waves on the Delay/Doppler altimeters: Analysis using real Sentinel-3 data. In Proceedings of the Ocean Surface Topography Science Team Meeting 2020, Virtual, 19–23 October 2020. Available online: https://ostst.aviso.altimetry.fr/fileadmin/user_upload/tx_ausyclsseminar/files/TranetAl_DopplerWaves_DataAnalysis_OSTST_2020.pdf (accessed on 1 October 2024).
129. Buchhaupt, C.; Egido, A.; Smith, W.H.F.; Fenoglio, L. Conditional sea surface statistics and their impact on geophysical sea surface parameters retrieved from SAR altimetry signals. *Adv. Space Res.* **2023**, *71*, 2332–2347. [CrossRef]
130. Buchhaupt, C.K.; Egido, A.; Vandemark, D.; Smith, W.H.F.; Fenoglio, L.; Leuliette, E. Towards the mitigation of discrepancies in sea surface parameters estimated from low- and high-resolution satellite altimetry. *Remote Sens.* **2023**, *15*, 4206. [CrossRef]
131. Abdalla, S.; Dinardo, S. Does Swell Impact SWH from SAR Altimetry? In Proceedings of the SAR Altimetry Workshop 2016. La Rochelle, France, 31 October 2016. Available online: https://ostst.aviso.altimetry.fr/fileadmin/user_upload/tx_ausyclsseminar/files/SAR_03_Abdalla_SAR_WS_20161031.pdf (accessed on 1 October 2024).
132. Moreau, T.; Tran, N.; Aublanc, J.; Tison, C.; Le Gac, S.; Boy, F. Impact of long ocean waves on wave height retrieval from SAR altimetry data. *Adv. Space Res.* **2018**, *62*, 1434–1444. [CrossRef]
133. Reale, F.; Pugliese Carratelli, E.; Di Leo, A.; Dentale, F. Wave orbital velocity effects on radar Doppler altimeter for sea monitoring. *J. Mar. Sci. Eng.* **2020**, *8*, 447. [CrossRef]
134. Egido, A.; Buchhaupt, C.; Boy, F.; Maraldi, C.; CLS Team. Correcting for the Vertical Wave Motion Effect in S6-MF Observations of the Open Ocean. In Proceedings of the Ocean Surface Topography Science Team Meeting 2022, Venice, Italy, 31 October–4 November 2022. Available online: https://ostst.aviso.altimetry.fr/fileadmin/user_upload/OSTST2022/Presentations/IPM2022-A_Significant_Wave_Height_Correction_to_Account_for_Vertical_Wave_Motion_Effects_in_SAR_Altimeter_Measurements.pdf (accessed on 1 October 2024).
135. Amarouche, L.; Tran, N.; Pirotte, T.; Mrad, M.; Etienne, H.; Moreau, T. Analysis of waves dynamics impact on Sentinel-6MF delay/Doppler measurements. In Proceedings of the Ocean Surface Topography Science Team Meeting 2023, Puerto Rico, WV, USA, 20 October 2023. Available online: https://ostst.aviso.altimetry.fr/forum-pages/fileadmin/user_upload/OSTST2023/Presentations/IPC2023-Analysis_of_Waves_Dynamics_Impact_on_Sentinel-6MF_Delay_Doppler_Measurements.pdf (accessed on 1 October 2024).
136. Buchhaupt, C.; Fenoglio, L.; Becker, M.; Kusche, J. Impact of vertical water particle motions on focused SAR altimetry. *Adv. Space Res.* **2021**, *68*, 853–874. [CrossRef]
137. Marié, L.; Nouguier, F.; Vandemark, D.; Ardhuin, F.; Chapron, B. On the effects of ocean surface motion on delay-Doppler altimetry. *IEEE Trans. Geosci. Remote Sens.* **2024**, *62*, 4207725. [CrossRef]
138. Bignalet-Cazalet, F.; Roinard, H.; Pirotte, T.; Picard, B.; Homerin, A.; Kientz, N.; de la Flèche, A.; Maraldi, C.; Raynal, M.; Picot, N. Calibration and validation performance assessment for SWOT's nadir altimeter. 2024; *in preparation*.